Aquatic Botany 184 (2023) 103592

Contents lists available at ScienceDirect

Aquatic Botany

journal homepage: www.elsevier.com/locate/aquabot

Review

Areal extent of vegetative cover: A challenge to regional upscaling of methane emissions

John M. Melack[a,b,c,*], Laura L. Hess[a]

[a] Earth Research Institute, University of California, Santa Barbara, CA, USA
[b] Bren School of Environmental Science and Management, University of California, Santa Barbara, CA, USA
[c] Department of Ecology, Evolution and Marine Biology, University of California, Santa Barbara, CA, USA

ARTICLE INFO

Keywords:
Remote sensing
Synthetic aperture radar
Lidar
Optical sensors
Northern wetlands
Tropical wetlands
Inundation
Aquatic plants

ABSTRACT

Given the influence of aquatic plants on methane production and emission and the challenges of regional upscaling, advances in remote sensing capabilities for mapping wetland vegetation and inundation are reviewed. Sensors used for remote sensing have varied imaging mode (passive or active), wavelength range (visible to microwave), platform (aircraft or satellite-borne), and spatial and temporal resolutions. Green and senescent vegetation, some vegetation assemblages and foliar chemistry can be detected from spectral curves in visible and infrared wavelengths. Backscattered signals from synthetic aperture radar (SAR) sensors can detect flooding beneath plant canopies, identify structural features of vegetation and penetrate cloud cover. Lidar permits mapping of topography and vertical structure of vegetation. A comprehensive, global dataset of areal coverage of major wetland types and their variability relevant to methane emissions does not exist, and regional datasets provide only broad categories of aquatic plants and limited information on seasonal variations in areal extent or inundation. Validated SAR-based maps for the Amazon basin offer areal estimates of seasonally flooded forests, seasonally flooded savannas and other interfluvial wetlands, herbaceous plants on riverine floodplains and peatlands. Other large regions for which areal estimates are available include the Pantanal (South America), Congo basin and Sudd (Africa), China, Europe, the continental U.S., and northern wetlands in Canada, Alaska and Russia. Active efforts to map the extent and changes in vegetation and inundation promise advances in understanding the role of aquatic plants in methane biogeochemistry and fluxes, though significant research needs exist.

1. Introduction

Aquatic plants represent considerable taxonomic and ecological diversity (Sculthorpe, 1967; Hutchinson, 1975; Wetzel, 2001) and contribute in several ways to methane emissions. Photosynthetic carbon dioxide fixation adds organic carbon to wetlands that fuels methane production by providing substrates and by influencing redox conditions (Whiting and Chanton, 1993; Mitsch and Gosselink, 2000; Schlesinger and Bernhardt, 2013). Plant-mediated transport of methane occurs via herbaceous and woody plants (e.g., Dacey, 1981; Villa et al., 2020; Barba et al., 2019; Covey and Megonigal, 2019). As reviewed by Bodmer et al. (2022), methane fluxes from vegetated areas are highly variable owing to both plant-mediated fluxes and water-to-atmosphere exchanges influenced by the plants. Hence, improved understanding of the roles of aquatic plants in methane fluxes is needed for mechanistic modeling and extrapolation to regional or global estimates.

Though many studies have investigated biogeochemical and ecological aspects of methane production, consumption and emission (e.g., Segers, 1998; Le Mer and Roger, 2001; Bridgham et al., 2013), upscaling to regional or larger scales remains elusive. A particular challenge is incorporation of spatial extent of aquatic plants, and its temporal changes. Given that emissions of methane from inland aquatic ecosystems are large and highly variable (Saunois et al., 2020; Rosentreter et al., 2021), and with the recent jump in atmospheric methane concentrations (Dlugokencky, 2021), improved understanding of the role of aquatic plants and wetlands (Sjögersten et al., 2014) is needed and timely.

Perspectives offered by a workshop sponsored by the International Geosphere-Biosphere Programme to identify data and research needs for characterizing wetlands in terms of their role in biogeochemical and

* Corresponding athor at: Earth Research Institute, University of California, Santa Barbara, CA, USA.
E-mail address: melack@bren.ucsb.edu (J.M. Melack).

https://doi.org/10.1016/j.aquabot.2022.103592
Received 2 July 2022; Received in revised form 2 October 2022; Accepted 14 October 2022
Available online 19 October 2022

hydrologic cycles remain relevant (Sahagian and Melack, 1998). A parameterization scheme, developed jointly by field ecologists and remote sensing experts, based on observable quantities to improve understanding of production and release of gases such as methane and carbon dioxide was proposed. If implemented, the functional parameterization would permit division of wetlands into functional types relevant to biogeochemical cycles. Our review builds on these perspectives with the benefit of 25 more years of advances in remote sensing and ecological and biogeochemical understanding. Remote sensing allows mapping of inundation and aquatic vegetation at local, regional, and perhaps global scales (Melack, 2004; Silva et al., 2015; Gomes et al., 2020; Ustin and Middleton, 2021). However, upscaling remains challenging owing to the dynamic and heterogeneous nature of aquatic plants and of inundation and cloud cover during key phenologic stages.

Our review provides an overview of remote sensing capabilities for mapping aquatic vegetation and inundation, highlights recent progress that has improved those capabilities, and examines case studies illustrating recent advances. We consider key aspects, including the extent, type and seasonality of broad categories of aquatic plants identifiable with regional remote sensing. In general, trees and herbaceous vegetation can be detected and distinguished. We focus on natural, inland wetlands, do not include phytoplankton, and provide only key references to coastal wetlands, mangroves and cultivated rice. We conclude by identifying remaining challenges and research needs. We do not review estimates of methane fluxes for each of the major regions with regional remote sensing estimates of areal coverage of aquatic habitats, but do cite summaries of fluxes for tropical and northern regions. The complementary review by Bastviken et al. (2022) focuses on processes relevant to methane production and flux at the ecosystem scale including sources of organic carbon, transport routes, and modulation of methane oxidation.

2. Remote sensing systems

Sensors used for remote sensing may be grouped by their imaging mode (passive or active), wavelength range (visible to microwave), platform (aircraft or satellite-borne), and spatial and temporal resolutions. Passive sensors measure reflected sunlight or emitted thermal or microwave radiation, while active sensors, such as radar or lidar, generate their own microwave or light pulses and receive the returned signals. Wavelengths employed in remote sensing range from the visible (~0.38–0.75 μm), through the near-infrared (~0.75–1.4 μm) and short-wavelength infrared (~1.4–3 μm), to the microwave (~5 mm - 100 cm). The wavelength ranges for synthetic aperture radar (SAR) commonly used for environmental remote sensing are called X-band (~3 cm), C-band (~5.5 cm), L-band (~23.5 cm), and P-band (~70 cm).

Tables 1 and 2 list several satellites and sensors used for mapping and monitoring wetland extent, vegetation, and inundation. Some legacy sensors are included owing to their importance for documenting long-term changes. The Committee on Earth Observation Satellites maintains a database of Earth observation instruments, searchable by mission, instrument, measurement, agency, or dataset (https://database.eohandbook.com/). Although we emphasize satellite-borne instruments used for regional mapping, analogous aircraft- or drone-based sensors are used for mapping smaller regions, algorithm or instrument development, and for validation of regional products.

Land cover classes such as water, green vegetation, senescent vegetation, and soil have distinctive spectral curves in visible and infrared wavelengths (Fig. 1). Water has very low reflectance in the near- and shortwave-infrared range, allowing discrimination between water and other land covers. Because chlorophylls and other leaf pigments strongly absorb sunlight in the visible wavelengths, green vegetation has low reflectance in the visible region. In the near-infrared, strong scattering from cell walls within the leaf mesophyll results in a distinctive shift from low to high reflectance between red and infrared wavelengths, known as the red edge; reflectance then drops in the shortwave infrared

Table 1
Selected optical satellite sensors relevant to study of aquatic vegetation.

Satellite	Sensor	Spatial resolution (m)	Bands[1] and Modes[2]	Repeat cycle (days)	Years operational
Optical, Moderate Resolution					
NOAA 1–16	AVHRR	1000	1 VIS, 1 NIR, 1 SWIR	1	since 1981
Terra, Aqua	MODIS	250–1000	10 VIS, 3 NIR, 3 SWIR	3	since 1999
Envisat	MERIS	300–1200	9 VIS, 2 NIR	3	2002–2012
Suomi NPP; NOAA-20	VIIRS	400–1600	5 VIS, 1 NIR, 5 SWIR, 3MWIR, 4 LWIR	1	since 2011
PROBA-V	Vegetation Instrument	333–667	2 VIS, 1 NIR, 1 SWIR	1–2	since 2013
Sentinel-3A	OLCI	300–1200	7 VIS, 3 RE, 3 NIR	2	since 2016
Optical, Fine Resolution					
Landsat 1–3	Multispectral Scanner	60	2 VIS, 2–3 NIR	18	1972–1983
Landsat 4–5	Thematic Mapper	30	3 VIS, 1 NIR, 2 SWIR	16	1982–2011
Landsat 7	Enhanced Thematic Mapper Plus	15–30	3 VIS, 1 NIR, 2 SWIR, 1 Pan	16	1999–2003
Landsat 8,9	Operational Land Imager	15–30	4 VIS, 1 NIR, 2 SWIR, 1 Pan	16	since 2013
Sentinel-2A, 2B	MSI	10–20	4 VIS, 3 RE, 3 NIR, 2 SWIR	5	since 2015
Optical, Very Fine Resolution					
QuickBird	MS Scanner; Pan Camera	0.6–2.4	3 VIS, 1 NIR, 1 Pan	≤ 3	2001–2015
WorldView	WV60; SpaceView	0.3–0.5	5 VIS, 2 NIR, 1 RE, 1 Pan	1–3	since 2007
RapidEye	REIS	5	3 VIS, 1 NIR, 1 RE	1–6	since 2009
Pléiades	HiRI	0.5–2	3 VIS, 1 NIR, 1 Pan	26	since 2011
Cubesat	PlanetScope Dove	3	3 VIS, 1 NIR	1	since 2013

1. Optical band abbreviations: VIS - Visible; NIR - Near Infrared; SWIR - Shortwave Infrared; LWIR - Longwave Infrared; RE - Red Edge; Pan - Panchromatic. Optical bands for aerosols, water vapor, and cirrus are not listed. 2. Single-pass stereo capability

owing to absorption by leaf water (Silva et al., 2008). Non-photosynthetic vegetation (NPV) refers to senescent leaves and stems, as well as woody trunks and branches. NPV has lower near-infrared and higher shortwave infrared reflectance than green vegetation, but can be difficult to distinguish from soil, depending on soil texture, organic matter and water content, and mineral composition. Endmember spectral mixing models can be used to distinguish fractional areas of particular plant assemblages (Sadro et al., 2007; Somers et al., 2011). Hyperspectral sensors (Buckingham and Staenz, 2008) also allow detection of foliar chemistry (LaCapra et al., 1996; Asner, 1998; Kokaly et al., 2009).

Table 2
Selected active microwave satellite sensors relevant to study of aquatic vegetation.

Satellite	Sensor	Spatial resolution (m)	Bands and Modes[1]	Repeat cycle (days)	Years operational
Active Microwave (Synthetic Aperture Radar; SAR), Very Fine to Moderate Resolution					
JERS-1	SAR	12.5	L-band; HH pol	45	1993–1997
RADARSAT-1,2	SAR	1–100	C-band; single-, dual-, or quad-pol	24	1995–2007
ALOS; ALOS-2	PALSAR; PALSAR-2	1–100	L-band; single-, dual-, or quad-pol	46; 14	2006–2011
TerraSAR-X, TanDEM-X	TerraSAR-X, TanDEM-X	3–40	X-band; single-, dual-, or quad-pol	11	since 2008
Sentinel-1	C-SAR	3.5–40	C-band; dual-pol	12	since 2014

1. Microwave polarization modes: single-, dual-, and quad-pol modes use one, two, or all of the four possible transmit-receive configurations: HH - horizontal transmit, horizontal receive; HV - horizontal transmit, vertical receive; VV - vertical transmit, vertical receive; VH -vertical transmit, horizontal receive.

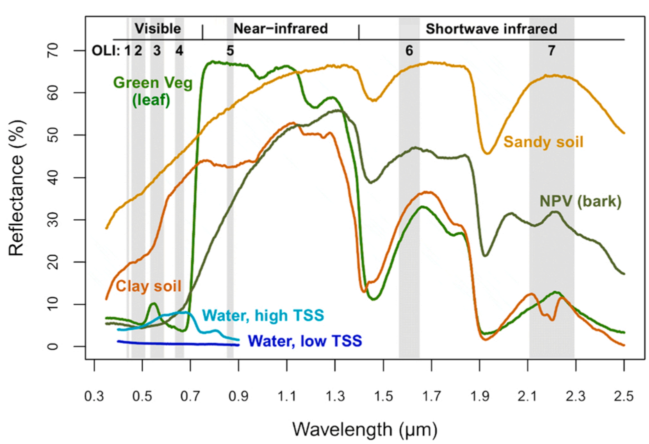

Fig. 1. Examples of visible and infrared spectral curves acquired by field spectrometry. Spectral response shown for green vegetation (single leaf), non-photosynthetic vegetation (NPV; bark), sandy soil, clay soil, and lake water with total suspended solids (TSS) concentrations of 1.9 mg/L and 20.8 mg/L. Band ranges of the Landsat 8 Operational Land Imager (OLI) in the visible (ultra-blue, blue, green, red; bands 1–4), near-infrared (NIR; band 5), and shortwave infrared (SWIR1, SWIR2; bands 6 and 7) portions of the spectrum shown as gray bars. Each curve represents one field sampling, and does not indicate variability within each class. Water spectra are from Novo et al. (2013). Land spectra compiled by Rebecca Powell, courtesy of VIPER Laboratory, University of Californa, Santa Barbara.
Reprinted with permission from Hughes, J., Clarkson, B.R., Castro-Castellon, A. T., Hess, L.L., 2019. Wetland plants and aquatic macrophytes. Pages 173–206 in J. Hughes (ed) Freshwater Ecology and Conservation: Approaches and Techniques. Oxford University Press, Oxford.

Synthetic aperture radar sensors have been widely used for wetland mapping because of their ability to detect flooding beneath plant canopies, identify structural features of vegetation, and penetrate cloud cover (Hess et al., 1990; Kasischke et al., 1997; Adeli et al., 2020). At wavelengths used by SAR sensors, transmitted microwave signals are backscattered by structural elements of vegetation: shorter wavelengths are scattered by smaller canopy elements such as leaves and small branches, while longer wavelengths are scattered by trunks and larger branches (Wang et al., 1995). The SAR signals include backscatter amplitude, phase, and polarization. Results from the SIR-C mission illustrate the utility of these three properties of SAR signals as applied to wetlands (e.g., Hess et al., 1995; Alsdorf et al., 2000). Double-bounce scattering, in which near-specular reflections between surface water and tree trunks yield enhanced returns, makes it possible to detect flooding beneath most forest canopies with L-band, and beneath herbaceous and savanna canopies with C-band (Hess et al., 2003; Silva et al., 2013). Interferometric applications of SAR can provide information about slopes and direction of movement of water across floodplains and wetlands (Alsdorf et al., 2005, 2007; Wdowinski and Hong, 2015; Liao et al., 2020), and subsidence of disturbed peatlands (Umarhadi et al., 2021).

SAR interferometry has been the primary approach used to produce global topographic data, which are fundamental to understanding wetland inundation and vegetation distribution. The C-band-based Shuttle Radar Topographic Mission (SRTM) DEM (digital elevation model), acquired in 2000, first released in 2003, and improved in later versions, has coverage between ~60^{o} north to south latitude at ~90 m horizontal resolution. It was the primary DEM used for the MERIT DEM (corrected to remove tree canopy bias; Yamazaki et al., 2017) and MERIT Hydro, a global hydrography dataset (Yamazaki et al., 2019). GFPLAIN, a map of global floodplains at 250 m resolution (Nardi et al., 2019), is also derived from SRTM. The Copernicus GLO30 DEM (from European Space Agency) was acquired with X-band TanDEM-X SARs from 2011 to 2015, and is available at 30 m horizontal resolution. Hawker et al. (2022) have provided a version corrected for forest and building heights. A limitation of global DEMs is the lack of topographic information for many seasonally variable floodplains: water depths below the surface at the time of the interferometric observations cannot be recovered. However, methods have been developed for recovering this information using other datasets (Fassoni-Andrade et al., 2020).

Time-series products derived from satellite-borne, passive microwave sensors have been used to determine seasonal variations in inundated areas for large regions (at ~25-km scale) without dense forest cover (Sippel et al., 1994). Emissivities and brightness temperatures detected by passive microwave radiometers are sensitive to the presence of surface water because of different dielectric properties of water, soil and vegetation. For example, Hamilton et al., (2002, 2004) used this approach to determine monthly inundation in large South American wetlands and extended the records for decades using regressions between flooded area and river stage heights. The Global Inundation Extent from Multi-Satellites dataset (GIEMS; Prigent et al., 2020) used data from several sensors to generate monthly estimates of global surface water extent over the last 25 years; Prigent et al. (2007) and Papa et al. (2010) provide other applications of the approach. Aires et al. (2013) used the 25-km resolution products in conjunction with SAR-based images to downscale inundation in the Amazon basin over a 15-year period to a resolution of about 500 m. Kitambo et al. (2022) combined GIEMS with altimetry to characterize the surface hydrology of the Congo basin, and its variability. Fluet-Chouinard et al. (2015) proposed another approach for a global inundation map based on topographic downscaling of coarse-scale remote sensing data. Schroeder et al. (2015) and Jensen and McDonald (2019) describe a monthly, global inundation product using AMSR-E (passive microwave) and QSCAT (radar scatterometry) data at 0.25^{o} resolution. Parrens et al. (2019) used a combination of L-band passive microwave, optical and SAR datasets to produce a 1-km inundation product for the Amazon basin.

Gravity anomalies detected by the GRACE satellites can detect changes in water mass associated with seasonal variations in inundation at a scale of 10^4 to 10^5 km^2 (e.g., Alsdorf et al., 2010; Xavier et al., 2010). Though spatially coarser than other techniques, some regional estimates and models of methane fluxes associated with wetlands use GRACE-based information (e.g., Basso et al., 2021). Lee et al. (2011) combined GRACE with altimetry to calculate water storage and inundation for floodplains and wetlands in the Congo basin.

A relatively new technique for radar-based detection of sub-canopy inundation is known as GNSS-reflectometry (GNSS-R; Jensen et al., 2018). In contrast to SAR systems, where signals are sent and received by the same instrument (i.e., monostatic systems), GNSS-R employs a bistatic concept in which reflected L-band transmissions from Global Navigation Satellite Systems (e.g., GPS, GLONASS, Galileo) are received by other satellites such as CYGNSS (NASA's Cyclone GNSS). Although GNSS-R has not been widely validated for wetlands, initial results indicate the potential of the technique for mapping inundated vegetation at coarse spatial but fine temporal resolution (Morris et al., 2019; Chapman et al., 2022).

Lidars for Earth observation are active optical sensors that transmit light at green or near-infrared wavelengths and measure returned light energy either as a full waveform or as discrete returns from waveform peaks. Airborne lidars have been used for mapping topography and bathymetry of coastal wetlands (Brock et al., 2002; Mandlburger, 2020) and river floodplains (Resop et al., 2019), and airborne lidar measurements of forests have advanced knowledge of forest vertical structure (Beland et al., 2019). The ICESat/GLAS satellite was used to map global forest canopy height at 1 km resolution (Simard et al., 2011), and to create high-resolution regional maps of mangrove canopy heights

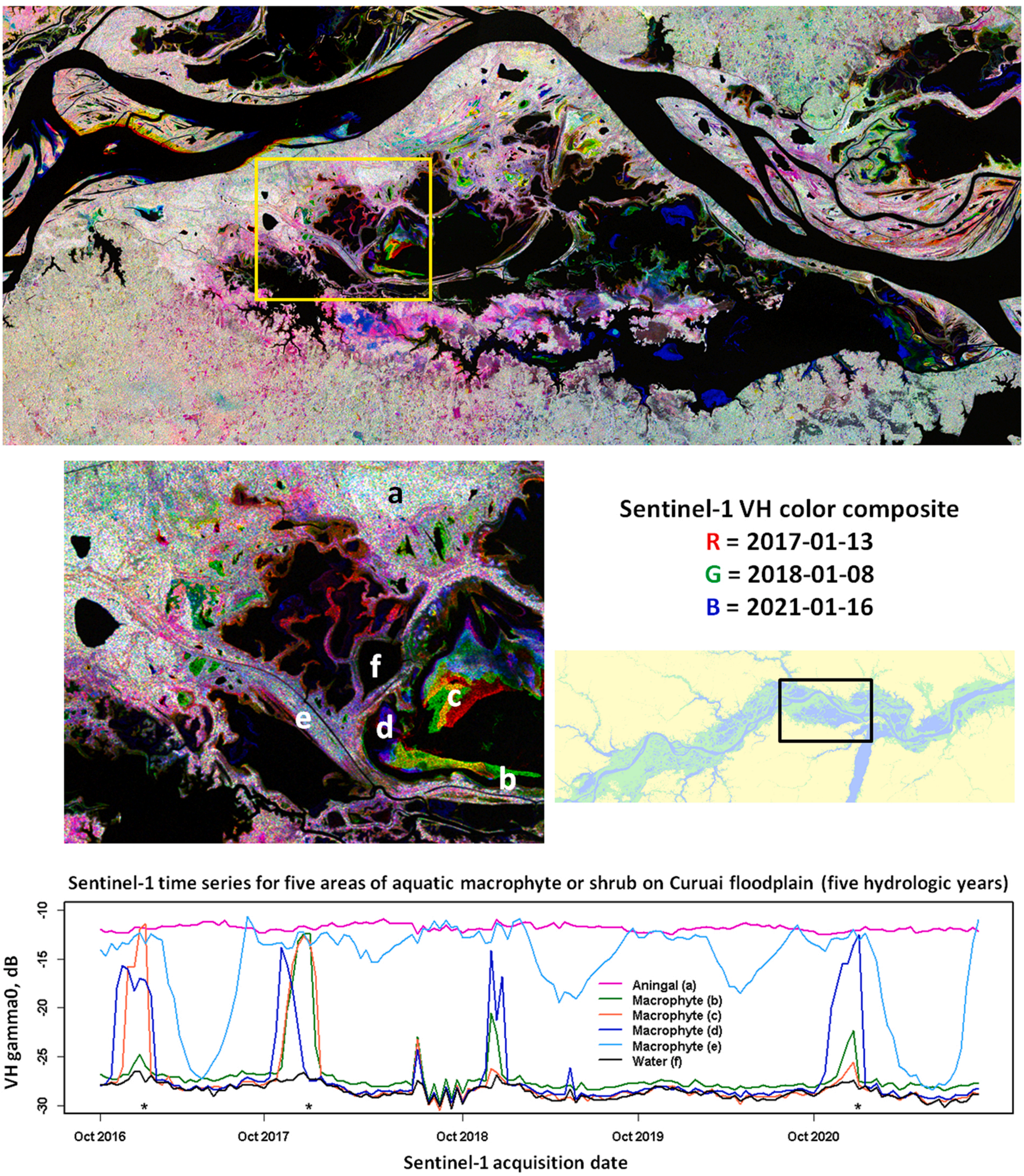

Fig. 2. Sentinel-1 color composite (early January 2017, 2018, 2021) and five-year time series (October 2016 - September 2021) of VH radar backscattering for wetland habitats of Curuai floodplain. Seasonal and internannual variability of aquatic macrophyte stands (primarily floating grasses) contrast with nearly constant backscattering from 'aningal' shrub stands (primarily *Montrichardia* sp.). Copernicus Sentinel-1 data obtained from Alaska Satellite Facility.

(Fatoyinbo and Simard, 2013). NASA's GEDI lidar, mounted on the International Space Station, has collected lidar data since April 2019 (https://gedi.umd.edu/instrument/instrument-overview/). The 25 m GEDI footprints are spaced along tracks separated by ~600 m; these have been combined with raster datasets such as Landsat to create high-resolution global maps of forest canopy height (Potapov et al., 2020). Verhelst et al. (2021) used GEDI data to improve the accuracy of forest vs. non-forest discrimination in Gabon wetlands. An important application of canopy height data is to remove the effective canopy height from digital elevation models to yield 'bare-earth' terrain models required for hydrologic modeling.

3. Advances and trends in remote sensing of wetlands and aquatic vegetation

Several recent publications review applications of remote sensing to wetlands and related hydrology (Silva et al., 2008; Adam et al., 2010; Klemas, 2013; Gallant, 2015; McCabe et al., 2017; Mahdavi et al., 2018; Wohlfart et al., 2018; Adeli et al., 2020; Fassoni-Andrade et al., 2021; Campbell et al., 2022). Tiner et al. (2015) includes chapters introducing remote sensing approaches plus many chapters with specific applications for sites distributed widely. In light of the numerous studies focusing on specific techniques or sites and the recent reviews, we have selected examples of recent advances with particular relevance to aquatic vegetation to highlight.

3.1. Wetland habitat mapping and monitoring using radar and optical time series

The European Space Agency's Sentinel-1 satellites have been acquiring high-resolution C-band SAR data with a 12-day repeat cycle since 2016. The free availability of time series of systematically acquired SAR data at a high temporal frequency is a major advance for remote sensing of aquatic vegetation. A multi-year color composite of C-HV Sentinel-1 IW mode scenes for the Curuai floodplain along the Amazon River and a five-year time series showing the distribution of herbaceous aquatic vegetation (Fig. 2) indicate the considerable interannual variability and spatial heterogeneity of these plants, which can only be captured by multi-year observations at regular, frequent intervals. From these observations, images of mean, standard deviation, minimum and maximum, and quantiles of radar backscatter can be produced (Fig. 3) with substantially reduce radar speckle. Such layers are suitable for image segmentation and object-based classification to map habitat types with better accuracy than can be achieved using a limited number of dates. Sentinel-1 time-series data are also being used in other regions to monitor dynamics of water bodies in wetlands (Borah et al., 2018; Schlaffer et al., 2022), and to map aquatic herbaceous vegetation (Zhang et al., 2022) and paddy rice (Bazzi et al., 2019). Canisius et al. (2019)

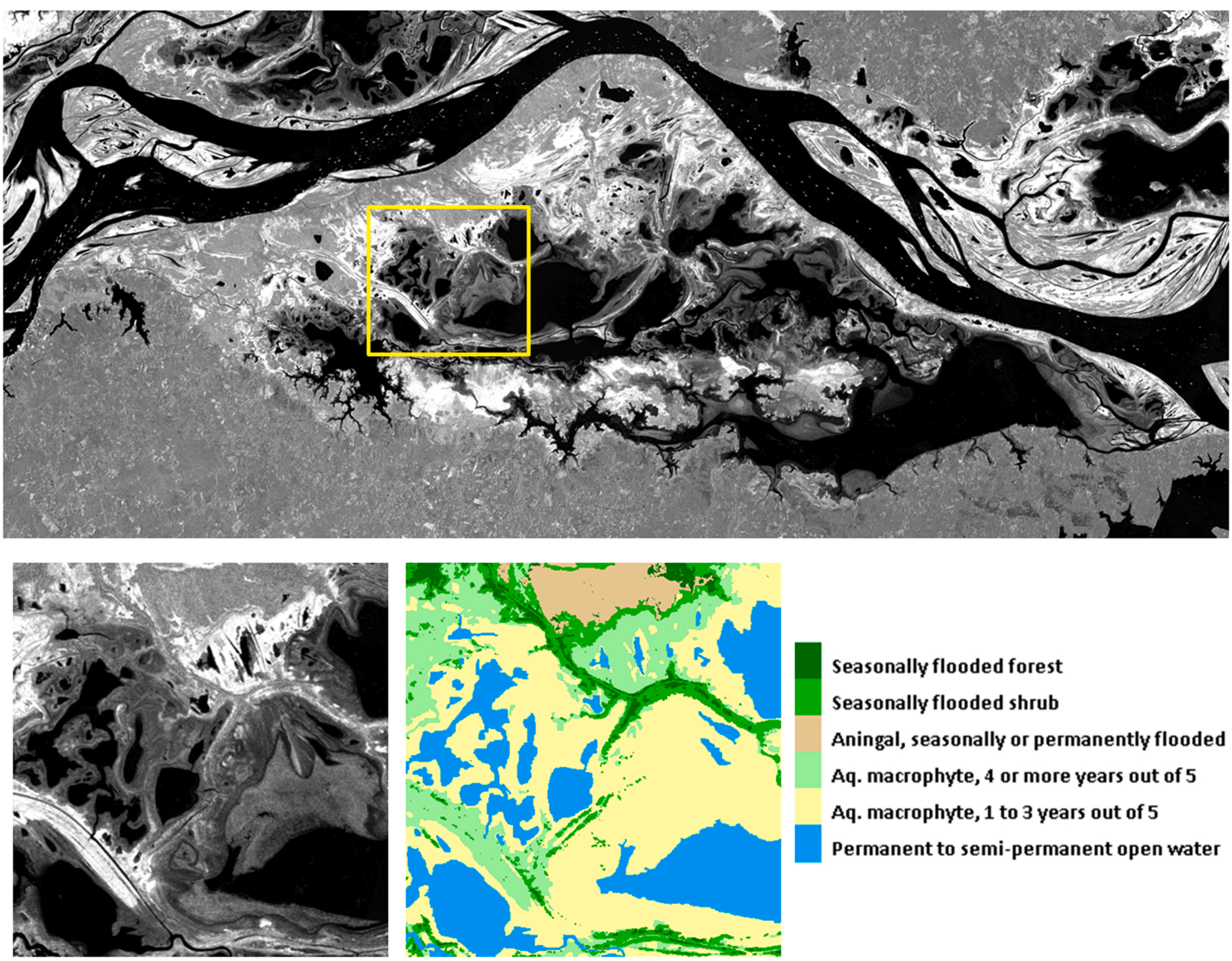

Fig. 3. Five-year standard deviation of Sentinel-1 VH backscatter for Curuai floodplain along Amazon River, and habitat map at 30 m resolution as inset. Object-based classification inputs are 5-year mean (156 observations), standard deviation, minimum, and maximum of VH backscatter, and the Copernicus GLO-30 DEM.

mapped floodplain vegetation and inundation dynamics at an Amazon floodplain site using time series of Radarsat-2 backscatter and InSAR coherence, and Chen et al. (2020) used Radarsat-2 and Sentinel-1 backscattering and coherence to map phenology and water levels in North American Great Lake coastal marshes. Furthermore, where cloud cover does not limit the availability of cloud-free observations, time series of high-resolution optical data are effective for mapping wetland habitats. Examples include mapping floodplain grasses using Sentinel-2 (Rapinel et al., 2019) and assessing long-term changes in bogs, fens, and marshes using Landsat (Mahdianpari et al., 2020a).

3.2. Use of very high resolution imagery

Very high-resolution imagery (< 5 m) from commercial vendors (Table 1), is valuable for training and validation of medium-resolution image classifications and for site-specific studies (Lesiv et al., 2018; Maciel et al., 2020; Amaral et al., 2021; Mateo-Garcia et al., 2021). Such imagery has become increasingly available as constellations of CubeSats make it possible to provide composited, cloud-free images even in cloudy regions. The Norway International Climate and Forests Initiative (NICFI; https://www.planet.com/nicfi/) provides freely available monthly composites of PlanetScope 5 m visible and near-infrared satellite imagery for the tropics for non-commercial use. NICFI data provide a high-resolution view of the extent and phenologic state of herbaceous aquatic plants and inundated forests over remote regions even at times of year when cloud-free optical data such as Landsat or Sentinel-2 are not available (Fig. 4). To calculate methane fluxes from coastal forested wetlands, Hondula et al. (2021) estimated surface water extent using daily time series of 3 m PlanetScope imagery. Another approach to acquisition of very high-resolution images is provided by Palace et al. (2018) who used a simple RGB camera mounted on a fixed-wing drone to map vegetative cover at 0.03 m resolution for plants related to methane production in a palsa peatland (northern Sweden).

3.3. Combinations of remote sensing data

Combining data from optical and SAR sensors enhances characterization of wetlands and aquatic plants, with many examples for a variety of regions. Betbeder et al. (2013), Bourgeau-Chavez et al. (2015), Margono et al. (2014), and Lee et al. (2015) combined PALSAR with optical data (Landsat or MODIS), while Slagter et al. (2020), Gašparović and Klobučar (2021), and Hosseiny et al. (2021) combined Sentinel-1 and Sentinel-2 data. Niculescu et al. (2020) provide a detailed evaluation of the accuracies with which reeds (*Phragmites australis*) and several other aquatic macrophyte species could be mapped in the Danube Delta using Sentinel-1 time series, or with various combinations of Sentinel-1, Sentinel-2, and Pléiades data. Bhatnagar et al. (2021) demonstrated the combination of drones and satellites to monitor wetlands. Hoyt et al. (2020) related remote sensing-based subsidence in southeast Asian peatlands to carbon emissions. Tulbure et al. (2022) consider the especially difficult challenge of detection of ephemeral wetlands.

Detection of submerged plants is difficult using remote sensing as the signal from the plants is influenced by surface reflectance and underwater attenuation by suspended and dissolved constituents. Santos et al. (2016) successfully used a time-series of data obtained with an airborne hyperspectral sensor to map spread of invasive submerged plants in the Sacramento-San Joaquin River Delta. Visser et al. (2018) flew a camera sensing in the visible and near-infrared on a drone and were able map submerged vegetation in a shallow river. Hydroacoustic systems have also been used to map submerged plant distributions and abundances as a complement to labor-intensive sampling (Valley et al., 2015). Validation with field observations is necessary and differences between hydroacoustic systems can occur (Radomsky and Holbrook, 2015).

4. Areal coverage of aquatic plants

A comprehensive, global dataset of areal coverage of major types of aquatic vegetation and their variability relevant to methane emissions does not exist. Although Davidson et al. (2018) identified 19 estimates of global wetland area, the estimates did not distinguish types of vegetation. Furthermore, aquatic vegetation varies widely as evident in the multiple wetland classification schemes proposed (summarized in Tiner, 2015). Bottom-up assessments of wetland areas are derived from site-level descriptions and national inventories (available for only about half the countries) and cover only a selection of major wetlands, often with poor coverage of floodplains. Top-down, global assessments are based largely on optical satellite remote sensing with inherent limitations for some regions and for forested wetlands. For example, the GlobCover land cover, 300-m product, based on surface reflectance mosaics of the Medium Resolution Imaging Spectrometer, is known to considerably under-estimate flooded vegetation (Bontemps et al., 2011). Xu et al. (2022) demonstrate an approach using several types of data (optical, SAR and lidar remote sensing products plus topographic, soils and climate data) to generate global coverage of a three types of aquatic vegetation (trees, shrubs, herbaceous cover) for one year, but without seasonal variations. The Copernicus Global Land Service: Land Cover 100-m dataset (CGLS-LC100), updated annually, includes a herbaceous wetland class (Buchhorn et al., 2020; https://land.copernicus.eu/global/products/lc). However, map accuracies for the herbaceous wetland class for years 2015–2019 were consistently less than 65% (Tsendbazar et al., 2021). Liu et al. (2021) compared three current global 30-m land-cover products. Two have wetland classes that do not distinguish between woody and herbaceous cover; the FROM_GLC dataset includes marshland, mudflat, and marshland, and leaf-off classes though accuracies for wetlands classes are low.

International efforts, such as the GEO-Wetlands Initiative, are aiming to provide information from Earth observations to support the conservation and management of wetlands worldwide. Related activities motivated by the Ramsar Convention on Wetlands (Ramsar Convention on Wetlands, 2018) continue to generate improved national inventories. Table 3 lists on-going programs that include areal coverage of inland aquatic vegetation and wetlands for particular areas or vegetation types. Useful references or links with areal coverage and related aspects of coastal wetlands, cultivated rice and mangroves include Murray et al. (2022), Sea Grass Watch (https://www.seagrasswatch.org), Laborte et al. (2017), Torbick et al. (2017), Zhang et al. (2016a), (2016b), Mangrove Science (https://mangrovescience.org), Lucas et al. (2014), and Global Mangrove Watch (https://www.globalma.ngrovewatch.org), and the Mediterranean Wetlands Initiative (Perennou et al., 2018; https://medwet.org/). Several regional analyses of inland wetlands based on remote sensing are available, and we summarize findings for selected examples. In general, the results provide only broad categories of aquatic vegetation and limited information on seasonal variations in areal extent or inundation.

4.1. Amazon basin

Regionalization of methane fluxes in the Amazon basin is particularly challenging because of the large seasonal variations in aquatic habitats, the diversity of aquatic vegetation as well as the variability of methane fluxes. Melack et al. (2022) reviewed measurements of methane emissions and areal extents for streams and rivers, lakes, seasonally flooded forests, seasonally flooded savannas and other interfluvial wetlands, herbaceous plants on riverine floodplains, peatlands, and hydroelectric reservoirs throughout the Amazon basin. Variations in the amplitude, duration, frequency, and predictability of inundation were derived from remote sensing-based products, hydrological models and multi-source products (Fassoni-Andrade et al., 2021). Fleischmann et al. (2022) present an intercomparison of 29 inundation datasets for the Amazon basin and illustrate differences

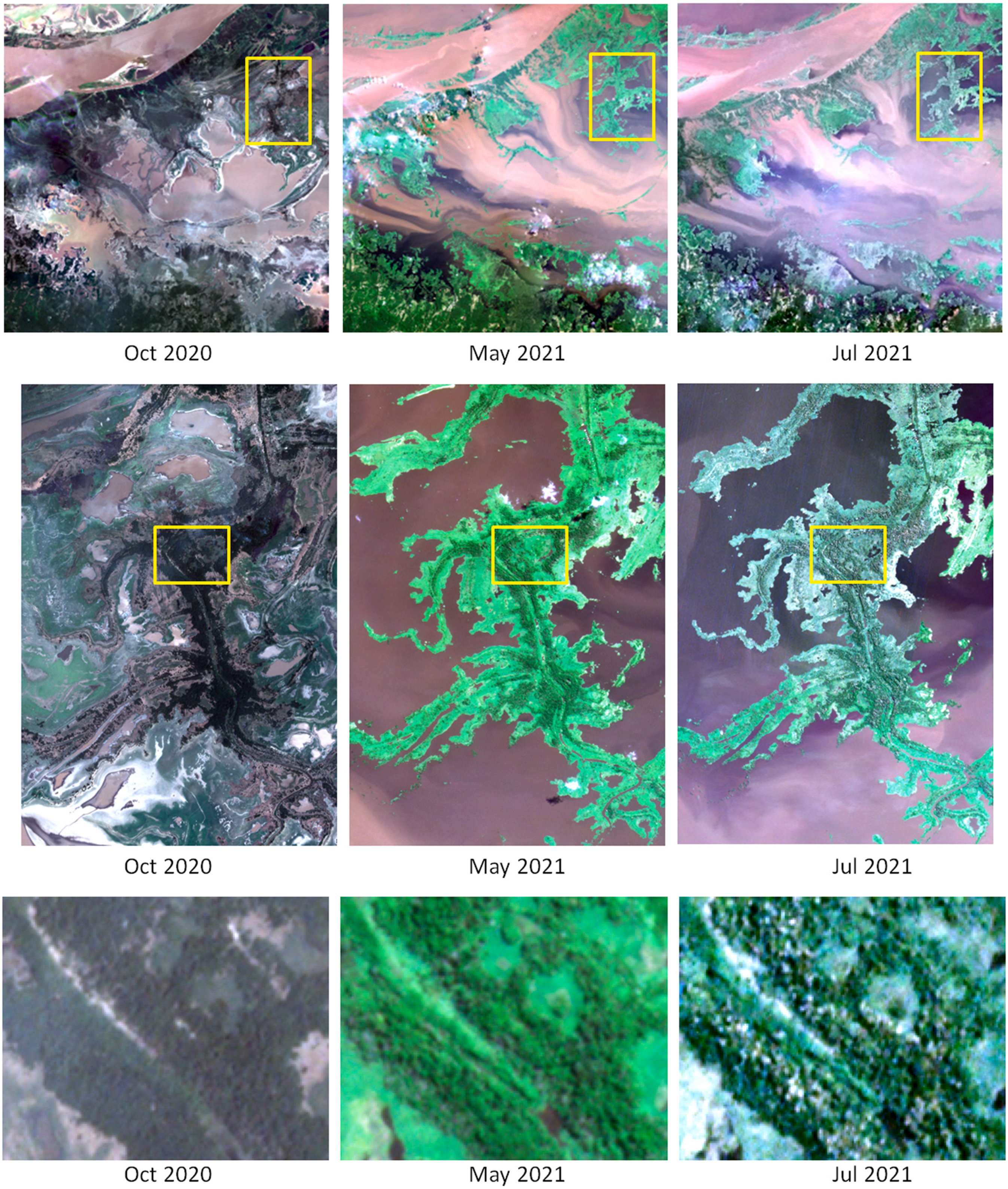

Fig. 4. Upper: mosaics of four Planet-NICFI quads (5 m PS Tropical Normalized Analytic Monthly Monitoring) for October 2020, May 2021, and July 2021, eastern Curuai floodplain (visible bands; near IR band also provided). Middle: close-up of delta for the same months, showing progression of aquatic herbaceous plants at low (October), high (May), and falling (July) water stages. After terrestrial phase of plant growth (October), stems grow rapidly with rising waters, to form floating mats (May). In July, beds are beginning to senesce. Lower: Forest and shrub on levee; woody canopies are green in October and May, and leafless crowns of flood-deciduous trees appear as light gray in July.

Table 3
Examples of wetland monitoring programs from GEO-Wetlands Initiative (www.earthobservations.org).

Program Name	Region	Website
GlobWetland-AFRICA	Africa	globwetland-africa.org
ESRD of Inundated Wetlands	Global	earthdata.nasa.gov/esds/competitive-programs/measures/an-inundated-wetlands-esdr
Satellite-based Wetlands Observation Service (SWOS)	Global	cordis.europa.eu/project/id/642088/fr
Sustainable Wetlands Adaptation and Mitigation Program (SWAMP) Global Wetlands	Global	www2.cifor.org/swamp/ www2.cifor.org/global-wetlands/
Copernicus Global Land Services (GLS)	Global	land.copernicus.eu/global/index.html
Copernicus Land Monitoring Services (CLMS): Water and Wetness HRL	European	land.copernicus.eu/pan-european/high-resolution-layers/water-wetness
Mediterranean Wetlands Observatory (MWO)	Mediterranean	tourduvalat.org/en/mediterranean-wetlands/mwo/
Interreg Balkan-Mediterranean WetMainAreas	Balkan Mediterranean	wetmainareas.com
Global Peatland Initiative	Global	www.globalpeatlands.org
International Peat Mapping	Indonesia	wri-indonesia.org/en/our-work/project/indonesian-peat-prize
Global Surface Water Explorer (GSWE)	Global	https://global-surface-water.appspot.com
Global Water Watch	Global	www.globalwaterwatch.io

among the products which vary in temporal (from static to monthly intervals, up to a few decades) and spatial (from 12.5 m to 25 km) resolutions. Differing characteristics of sensors, periods of acquisitions, spatial resolution, and data processing algorithms contribute to disparities with especially large uncertainties in the Llanos de Moxos and *campinas* and *campinaranas* in the Negro basin.

Though Junk et al. (2011) classified 14 major types of natural wetlands in the lowland Amazon, remote sensing cannot distinguish all types on a regional scale. Hess et al. (2003), Melack and Hess (2010) and Hess et al. (2015) used SAR imagery to map herbaceous and woody plants within floodable regions at a spatial resolution of about 100 m during high and low water levels. High-resolution airborne videography was used to validate the classifications (Hess et al., 2002). Remotely sensed products mapping aquatic vegetation are also available for subregions in the Amazon basin (e.g., Silva et al., 2010; Sartori et al., 2011; Hawes et al., 2012; Arnesen et al., 2013; Ferreira-Ferreira et al., 2015; Furtado et al., 2016; Pereira et al., 2018; Fonseca et al., 2019; Figs. 5 and 6).

Melack et al. (2022) provide estimates of the areal extent of major vegetated wetlands in the lowland Amazon: flooded forests reach maximum area of 442,000 km^2 (minimum area, ~33,000 km^2) of which up to ~84,000 km^2 are *igapó* forest along black-water rivers and up to ~50,000 km^2 occur near clear-water rivers. Venticinque et al. (2016) show the locations of white, black and clear water rivers. Seasonally inundated savannas with herbaceous plants, palms and trees occur in Roraima (maximum and minimum areas of 16,500 and 250 km^2), the Llanos de Moxos (maximum and minimum areas of 83,000 and 6100 km^2), and in the middle Negro basin (~30,000 km^2). Herbaceous plants often cover exposed sediments during low water and as rooted emergent and free-floating plants, as water levels rise (Junk and Piedade, 1997). Common plants include *Echinochloa polystachya, Paspalum repens, Paspalum fasciculatum*, *Hymenachne amplexicaulis*, *Oryza perennis*, and the genera *Eichhornia, Ludwigia, Neptunia, Salvinia,* and *Pistia* (Engle et al., 2008; Silva et al., 2013). Remotely sensed imagery can detect such herbaceous vegetation, though not distinguish among the species; time-series data are required because of the large seasonal changes, as illustrated in Fig. 3. At high water approximately 25,000 km^2 of herbaceous plants can occur (Melack and Hess, 2010; Hess et al., 2015). In floodplain lakes totaling ~9400 km^2 along the eastern Amazon River, herbaceous plants coverage ranged from 770 to 2900 km^2 over two years (Silva et al., 2013). Herbaceous plants are rarely abundant in black-water river systems, and are only moderately common in clear-water rivers (Junk et al., 2011). Draper et al. (2014) estimated that peatlands composed of seasonally flooded forests and palm swamps, cover 35,600 +/- 2130 km^2 in the Pacaya-Samiria region.

Significant methane fluxes from trees, especially when inundated, have been reported for the Amazon basin and elsewhere (Pangala et al., 2017; Sjögersten et al., 2020; Gauci et al., 2021). However, the large variability in these fluxes, diversity of trees, and difficulty of extrapolating to whole trees and then forests suggest that many more measurements are needed. Plant-mediated transport via herbaceous plants has not been consistently observed in Amazon wetlands (e.g., Wassmann et al., 1992; Bartlett et al., 1988; Oliveira Junior et al., 2020; Belger et al., 2011). As summarized in Melack et al. (2022), numerous measurements of methane fluxes are available from water within vegetated areas and hydrologically linked lakes and rivers.

4.2. Pantanal

The Pantanal wetlands, located in the center of South America with estimated inundated area of up to ~160,000 km^2, contain a large variety of alluvial ecosystems with differing inundation, geomorphology and vegetation types. To map this challenging diversity of habitats at a subregional scale, Evans et al. (2014) used 50-m, resolution, dual-season, L-band ALOS/PALSAR and C-band RADARSAT-2 data plus ground reference points, in a hierarchical object-based image analysis. They distinguished ten habitats with an overall accuracy of 80% for the entire Pantanal and provide areas and percent coverage for ten subregions and the entire Pantanal. In a representative region in the northern Pantanal, Arieira et al. (2011) used a four band IKONOS-2 image (4 m resolution) and SRTM DEM in conjunction with field surveys in a geostatistical analysis and ordination to identify and map seven vegetation types and relations between flood duration and vegetation zonation. Methane fluxes are available for only a few of the vegetation categories recognized in these studies (Hamilton et al., 1995, 2014; Marani and Alvala, 2007; Peixoto et al., 2015), though aircraft sampling provided an integrated regional estimate (Gloor et al., 2021).

4.3. African wetlands

Wetlands represent a considerable proportion of the Cuvette Centrale within the Congo River basin. Bwangoy et al. (2010) used imagery from the Landsat Thematic Mapper and Enhanced Thematic Mapper Plus sensors, JERS-1 L-band SAR imagery, and topographic indices derived from SRTM to develop a classification system that yielded an estimated wetland cover of 360,000 km^2 representing mostly flooded forest plus inundated grasslands. The Sudd (South Sudan) is a large wetland along the Nile River with limited information about its variable extent. Based on multiple 8-day composite, 500-m MODIS scenes, with high-resolution imagery used for validation, Di Vittorio and Georgakakos (2018) mapped the areas of permanently inundated regions vegetated with grasses, *Typha* and *Cyperus papyrus* (minimum area, ~12,500 km^2; maximum area, ~16,400 km^2) and seasonally flooded grasslands and woodlands (average area, ~15,000 km^2). Dambos, a widespread landform on elevated plateaus in eastern and central Africa and also present in the Sahel, include regions with seasonal saturated, vegetated soils. Based on studies in central Uganda, approximately 15% of the areas mapped by FAO-Africover as dambos are seasonal wetlands that emit methane (Sebadduka, 2014). Maps of wetlands in Kenya, Uganda, Tanzania and Rwanda are reviewed by Amler et al. (2015).

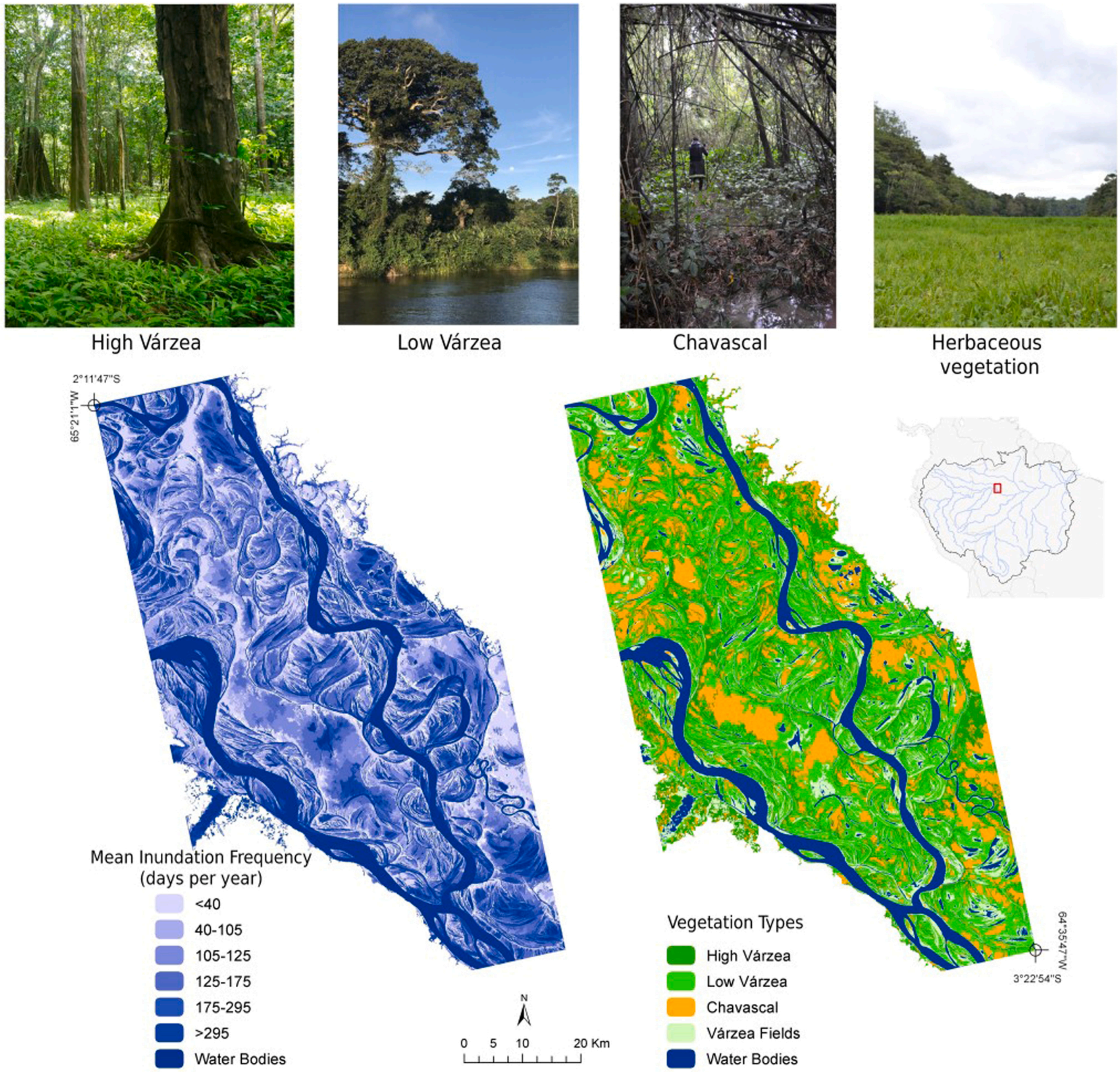

Fig. 5. Maps are based on a time series of ALOS/ PALSAR-1 data. Further information on remotes sensing analyses are in Ferreira-Ferreira et al. (2015). Wetland vegetation types and mean inundation frequency for portion of central Amazon floodplain between Solimões and Japurá rivers, Mamirauá area (adapted from Ferreira-Ferreira et al., 2015). Reproduced from Fassoni-Andrade et al. (2021).

4.4. China

A series of national wetland maps for China for 1978, 1990, 2000 and 2008 were developed using Landsat Multispectral Scanner, Landsat Thematic Mapper, Landsat ETM+ , and the China–Brazil Earth Resource Satellite (CBERS-02B CCD) imagery, respectively (summarized in Nui 2015). The classification system used 15 wetland types, but only two apply to natural inland wetlands. In 2008, seasonally and permanently inundated grasslands, shrubs, woodlands and forests covered ~144,150 km^2; the distribution of these wetlands and other types is provided as a map. The lumping of the considerable variety of aquatic vegetation and wetlands in this classification and lack of temporal information about inundation reduce its utility for upscaling of methane fluxes. The broad categories of wetlands with methane fluxes, as summarized in Xiao et al. (2019), would further limit the ability to recognize the influence of aquatic vegetation.

Poyang Lake, a large floodplain lake-wetland system along the lower Yangtze River, has been the focus of several innovative analyses. Of particular relevance are the application of the concept of plant functional groups to aquatic vegetation. By combining field surveys with time-series of multispectral satellite data, functional groups representing C3 grasses and forbs, C4 grasses and C3 reeds, and emergent and floating plants were distinguished and seasonally varying spatial maps produced (Dronova et al., 2012, 2015; Wang et al., 2012). Only a few measurements of methane flux for a subset of habitats are available for Poyang Lake (e.g., Wan et al., 2010; Hu et al., 2016).

4.5. Arctic and boreal areas

The Boreal–Arctic Wetland and Lake Dataset (BAWLD) is a land

Fig. 6. Aerial photograph of herbaceous aquatic plants (primarily *Paspalum repens*) and seasonally inundated forest, Mamirauá area.
Credit: Davy Rabelo (UEA).

cover dataset based on expert assessment and random forest modelling with spatial datasets of climate, topography, soils, permafrost conditions, vegetation, wetlands, and surface water (Olefeldt et al., 2021). Five wetland classes (bogs, fens, marshes, permafrost bogs, and tundra wetlands) at 0.5° resolution in northern boreal and tundra biomes (17% of the global land surface) are represented. Bog, fen, and permafrost bog are the most abundant wetland classes.

Alaska spans boreal and arctic regions with considerable wetland area. Mosaics of JERS-1 L-band SAR imagery were used by Whitcomb et al. (2009) to map vegetated Alaskan wetlands, most of which were classified as palustrine emergent herbaceous, scrub shrub or forest (based on the Cowardin et al., 1979 system). Clewley et al. (2015) combined L-band ALOS PALSAR and topographic data to generate an improved wetland map at 50 m resolution for Alaska with an accuracy for wetland classes of 85%. They estimated a total wetland area of 0.59×10^6 km^2 (36% of the total land area of Alaska).

Though regional datasets are essential for upscaling, fine spatial scale variability in methane fluxes among northern vegetated wetlands can be important (Davidson et al. (2016a). In an attempt to distinguish dominant tundra vegetation with spectroscopy, Davidson et al. (2016b) made field measurements on the North Slope of Alaska. They were able to separate vegetation communities within spectral regions of 450–510 nm, 630–690 nm and 705–745 nm at classification accuracies of 92–96%. Lower accuracies (~70%) were obtained with 2-m spatial resolution, multispectral WorldView-2 data.

Northern peatlands can be a significant wetland type and can be embedded in complex landscapes. Karlson et al. (2019) demonstrated the combination Sentinel-1 SAR and arctic digital elevation (ArcticDEM) data as inputs to random forest models to delineate peatlands, as well as water, forest and non-forest upland, in northern Sweden. Multi-seasonal SAR had user accuracy for peatlands of ~78%, and inclusion of terrain indices improved accuracy to ~88% with indices derived from the ArcticDEM.

The west Siberian lowland covers an area of 2.75×10^6 km^2 west of the Ural Mountains and east of the Yenisey River. Terentieva et al. (2016) conducted a supervised classification of Landsat imagery trained with high-resolution and field data for the whole region. They determined fractional coverage of seven wetland types (open water, waterlogged hollows, oligotrophic hollows, ridges, ryams, fens, palsa hillocks) with overall accuracy of 79%. A remaining challenge is adding variations in inundation as a result of snowmelt and rain.

The considerable variety among wetlands in Arctic and boreal regions is reflected in the variation in methane fluxes. Kuhn et al. (2021) summarize a dataset of CH_4 fluxes from 540 wetland and non-wetland and 1247 lakes and ponds. Their Boreal-Arctic Wetland and Lake Methane Dataset (BAWLDCH4) is linked to a land cover dataset with the same land cover classes to enable bottom-up estimates of methane fluxes. BAWLD-CH4 includes site-level CH_4 fluxes, measurement methods, timing, and frequency and site characteristics.

4.6. Canadian wetlands

Wetlands in Canada cover large areas and have been mapped using several satellite sensors into bogs, fens, marshes, swamps and shallow water. Amani et al. (2020) evaluated a Landsat-based inventory using in situ data, photo-interpreted products, land use maps and high-resolution aerial images, and identified limitations. In turn, Mahdianpari et al. (2020b); c) and Mahdianpari et al. (2021) describe three generations of inventories using optical and SAR sensors.

The first generation of these products mapped the whole country using an object-based, random forest classification approach at 10 m resolution with accuracies by province from 74% to 84%; 19% of land was classified as wetlands (Mahdianpari et al., 2020b). Sentinel-1 C--band (VV-VH and HH-HV polarization) SAR images acquired between June and August in 2016, 2017 and 2018 were used. To generate cloud-free Sentinel-2 images, three-month composites from June to August were used. Mahdianpari et al. (2020c) employed high-resolution optical data and visual interpretation to produce a second-generation map with accuracies from 76% to 91%. Further improvements in accuracies and areal extent were made by incorporating L-band ALOS-PALSAR-2 images, SRTM and arctic digital elevation models plus temperature, precipitation and night-time light data (Mahdianpari et al., 2021). Finer discrimination among vegetation types and time-series of inundation or soil moisture would further enhance the utility of these valuable products for upscaling methane fluxes.

4.7. Additional regional studies

Other regional wetland mappings are described by Bourgeau-Chavez et al. (2015) for coastal wetlands around the North American Great Lakes, Montgomery et al. (2021) for the prairie pothole region of North America, Perennou et al. (2018) for Mediterranean wetlands, Tanneberger et al. (2017) for peatlands in Europe, Margono et al. (2014) for Indonesia, Hess and Melack (2003) for tropical Australian floodplains, and Dahl (2011) for the conterminous United States.

5. Upscaling of methane fluxes with models and statistical analyses

As an aid to large-scale methane modeling, Zhang et al. (2021) developed the Wetland Area and Dynamics for Methane Modeling (WAD2M) dataset with 0.25° resolution (at the equator) and a monthly time step. WAD2M combines inundation derived from active and passive microwave remote sensing (SWAMPS, Jensen and McDonald, 2019) to represent spatial and temporal patterns of inundated and non-inundated vegetated wetlands; it excludes lakes, ponds, rivers, reservoirs, coastal wetlands and rice paddies. For situations where SWAMPS was not reliable, soil carbon or peatland (Hugelius et al., 2013; Gumbricht et al., 2017) or static wetland areas (Lehner and Döll, 2004) were used. In the Amazon basin, the hybrid expert system used by Gumbricht et al. (2017) is not consistent with other estimates of inundation (Fleischmann et al., 2022), perhaps because of over estimation of soil moisture by the topographic index used. Moreover, these products do not include types of aquatic vegetation.

The Wetland and Wetland CH_4 Inter-comparison of Models Project (WETCHIMP, Melton et al., 2013; Wania et al., 2013) demonstrated that the models included did not agree in their simulations of wetland extent or methane emission and had parameter and structural uncertainty. For example, maximum global wetland area used among the models ranged from 7.1 to 26.9×10^6 km^2, while observational estimates cited in Melton et al. (2013) ranged from 4.3 to 12.9×10^6 km^2. In comparison, Zhang et al. (2021) estimated a long-term, global maximum wetland area of 13×10^6 km^2. Moreover, current regional or global models of methane emissions from wetlands do not incorporate aquatic plants as functional groups or do so with broad categories. For example, Liu et al. (2020) used Mathews and Fung's (1987) classification of forested bog, non-forested bog, forested swamp, non-forested swamp and alluvial formations. Alluvial formations represented floodplains without the important differences among aquatic vegetation, as illustrated for the Amazon basin. Moreover, the areal coverage assigned to these broad categories do not have validated values with uncertainty estimates.

Most of the large-scale methane models use fairly coarse grids (commonly 0.5°) and drive methane fluxes based on simulated soil temperatures and carbon availability or heterotrophic respiration (e.g., JULES, Clark et al., 2011; LPJ-WSL, Zhang et al., 2016a, 2016b; LPX-Bern model, Ringeval et al., 2014; TEM-MDM, Liu et al., 2020; DLEM, Zhang et al., 2017; WetCHARTs, Bloom et al., 2017; JPL-WHyMe, Wania et al., 2010, and CLM4Me, Riley et al., 2011). Melack et al. (2022) compared an atmospheric transport model and mixing ratios available from field measurements to model ensembles available for WetCHARTs (Bloom et al., 2017). These comparisons indicated that WetCHART's fluxes for the region represented by the field data were too high, and that the seasonality of WetCHART-derived mixing ratios were one month out of phase when compared to the observations. Another important aspect of aquatic plants is their contribution of organic carbon as a substrate supporting methane production. However, with few exceptions (e.g., Potter, 1997; Potter et al., 2014), algorithms to estimate aquatic plant productivity are not included in these models.

The FLUXNET- CH_4 program has produced a multi-ecosystem dataset and analysis of methane seasonality from freshwater wetlands based on eddy covariance measurements (Delwiche et al., 2021). Using results from this program, Knox et al. (2021) applied statistical techniques to examine several physical and biological predictors of CH_4 fluxes. The sites included are mainly in northern regions with few tropical regions represented. Furthermore, the regions sampled by eddy covariance systems usually integrate several aquatic habitats, complicating attribution to specific types of aquatic vegetation.

6. Conclusion

The rich literature on aquatic plants and active efforts to map their extent and variations, as summarized above, promise important advances in understanding the role of aquatic vegetation in methane biogeochemistry and fluxes. Nevertheless significant limitations and needs exist. We highlight several research advances, challenges and directions.

One over-arching limitation and challenge in regionalization of methane fluxes is the lack of a comprehensive, global dataset of areal coverage of major types of aquatic vegetation and their variability. However, the technical feasibility of mapping aquatic vegetation at global scale has markedly improved in the past decade owing to several developments: 1) The systematic acquisition of multi-year time series of Sentinel-1 C-band SAR data at high (12-day) temporal resolution. Such time series allow accurate mapping of seasonal dynamics of open water, aquatic macrophytes, and some shrub and woodland wetland types. 2) Development of techniques for mapping wetland forests and their inundation patterns with L-band SAR, using JAXA's JERS-1 and ALOS PALSAR sensors. The NASA-ISRO NISAR mission (https://nisar.jpl.nasa.gov/) planned for launch in 2024 will allow application of these techniques at global scale using freely available, systematically acquired L-band time series at 12-day frequency. 3). Advances in cloud computing and machine learning, and increased use of open-source algorithms. Implementation of algorithms on platforms such as Google Earth Engine or Digital Earth Africa allows efficient generation of cloud-free time series of optical data from Landsat and Sentinel-2, which can be effectively combined with SAR data for land cover mapping. 4). Improved global DEMs. DEMs such as Copernicus GLO-30 have improved spatial resolution (~30 m vs. ~90 m), allowing better definition of complex wetland landforms. 5). Availability of extensive lidar measurements from the GEDI mission. Several global data sets have combined GEDI with optical and SAR data to produce forest height, woody biomass, and bare-earth elevation products. 6). Acquisition of composited very-high-resolution (~5 m) optical data from satellite constellations. Such high-resolution data sets, particularly when made freely available such as via the NICFI program, allow more rigorous validation and uncertainty estimation for aquatic vegetation maps throughout seasonal phenologic and hydrologic cycles.

While the Earth system modeling community has developed sophisticated, spatially-explicit models, aquatic vegetation is not well represented. Especially problematic are characterization of forest structure, a critical aspect of extrapolating methane fluxes from trees, and representing the variety of herbaceous vegetation.

A related aspect is the need to incorporate bare-earth DEMs with high vertical resolution as both hydrologic conditions and vegetation distributions are strongly related to topography.

In addition to characterization of areal extent of aquatic vegetation and inundation, the paucity of measurements of methane fluxes, especially ebullitive fluxes, fluxes through woody vegetation, and in many types of aquatic vegetation continue to constrain regional estimates of methane fluxes. Furthermore, modeling of methane fluxes requires better incorporation of the mechanisms producing, oxidizing and transporting methane. The recent review by Melack et al. (2022) provides examples of these and more limitations, using the Amazon basin as an example.

Given these significant advances, and the near-term expectation of freely available L-band data from NISAR, we suggest that the limitations to producing global data sets that accurately represent aquatic plants for input to methane models are likely to become more programmatic than technical in the near future. That is, adequate and consistent funding will need to be secured to do the complex but technically achievable classification and validation process involving large amounts of data. The groundwork for this endeavour can be laid by developing a consensus within the modeling community of the desired specifications for global or large-region products. Efforts, such as by the GEO Wetlands Initiative, to coordinate and integrate a variety of activities should aim for consistency in data formats and metadata and to increase the availability of the products and processing procedures. Better coordination between scientists addressing varied applications of wetlands remote sensing (Ramsar Convention, biodiversity, water resources, sustainable development, biogeochemistry, disaster assessment) would improve resource use efficiency and provide critical data to all communities. Finally, coordinated field campaigns that combine ground-based measurements with airborne and satellite acquisitions, such as LBA (Gash et al., 2009) and AboVE (https://above.nasa.gov/about.html), have proven their worth in maximizing scientific output derived from remote sensing products.

Declaration of Competing Interest

The authors declare that they have no known competing financial interests or personal relationships that could have appeared to influence the work reported in this paper.

Data Availability

No data was used for the research described in the article.

Acknowledgements

J.M.M. received support from NASA grant NNX17AK49G and the US National Science Foundation (Division of Environmental Biology, grant 1753856). L.L.H. was supported in part by the 2017–2018 Belmont Forum and BiodivERsA joint call 799 for research proposals under the BiodivScen ERA-Net COFUND program, and by the US National Science Foundation (International Global Change Research and Coordination, grant 1851993).

References

Adam, E., Mutanga, O., Rugege, D., 2010. Multispectral and hyperspectral remote sensing for identification and mapping of wetland vegetation: a review. Wetl. Ecol. Manag. 18, 281–296.

Adeli, S., Salehi, B., Mahdianpari, M., Quackenbush, L.J., Brisco, B., Tamiminia, H., Shaw, S., 2020. Wetland monitoring using SAR data: a meta-analysis and comprehensive review. Remote Sens. 12, 2190. https://doi.org/10.3390/rs12142190.

Aires, F., Papa, F., Prigent, C., 2013. A long-term high-resolution wetland dataset over the Amazon basin, downscaled from multiwavelength retrieval using SAR data. J. Hydromet. 14, 594–607.

Alsdorf, D., Han, S.-C., Bates, P., Melack, J., 2010. Seasonal water storage on the Amazon floodplain measured from satellites. Remote Sens. Environ. 114, 2448–2456.

Alsdorf, D., Dunne, T., Melack, J.M., Smith, L., Hess, L., 2005. Diffusion modeling of recessional flow on central Amazonian floodplains. Geophys. Res. Lett. 32, L21405. https://doi.org/10.1029/2005GL024412.

Alsdorf, D., Bates, P., Melack, J.M., Wilson, M., Dunne, T., 2007. Spatial and temporal complexity of the Amazon flood measured from space. Geophys. Res. Lett. 34, L08402.

Alsdorf, D.E., Melack, J.M., Dunne, T., Mertes, L.A.K., Hess, L.L., Smith, L.C., 2000. Interferometric radar measurements of water level change: Amazon floodplain response to river stage. Nature 404, 174–177.

Amani, M., Brisco, B., Mahdavi, S., Ghorbanian, A., Moghimi, A., DeLancey, E.R., Merchant, M., Jahncke, R., Fedorchuk, L., Mui, A., Fisette, T., Kakooei, M., Ali Ahmadi, S., Leblon, B., LaRocque, A., 2020. Evaluation of the Landsat-based Canadian wetland inventory map using multiple sources: challenges of large-scale wetland classification using remote sensing. IEEE J. Sel. Top. Appl. Earth Obs. Remote Sens 1, 32–52.

Amaral, J.H.F., Melack, J.M., Barbosa, P.M., Borges, A.V., Kasper, D., Cortes, A.C., Zhou, W., MacIntyre, S., Forsberg, B.R., 2021. Inundation, hydrodynamics and vegetation influences carbon dioxide concentrations in Amazon floodplain lakes. Ecosystems. https://doi.org/10.1007/s10021-021-00692-y.

Amler, E., Schmidt, M., Menz, G., 2015. Definitions and mapping of East African wetlands: a review. Remote Sens. 7, 5256–5282. https://doi.org/10.3390/rs70505256.

Arieira, J., Karssenberg, D., de Jong, S.M., Addink, E.A., Couto, E.G., Nunes da Cunha, C., Skøien, J.O., 2011. Integrating field sampling, geostatistics and remote sensing to map wetland vegetation in the Pantanal, Brazil. Biogeosciences 8, 667–686.

Arnesen, A.S., Silva, T.S.F., Hess, L.L., Novo, E.M.L.M., Rudorff, C.M., Chapman, B.D., et al., 2013. Monitoring flood extent in the lower Amazon River floodplain using ALOS/PALSAR ScanSAR images. Remote Sens. Environ. 130, 51–61. https://doi.org/10.1016/j.rse.2012.10.035.

Asner, G.P., 1998. Biophysical and biochemical sources of variability in canopy reflectance. Remote Sens. Environ. 64, 234–253.

Barba, J., Bradford, M.A., Brewer, P.E., Bruhn, D., Covey, K., Van Haren, J., Megonigal, J. P., Mikkelsen, T.N., Pangala, S.R., Pihlatie, M., Poulter, B., Rivas-Ubach, A., Schadt, C.W., Terazawa, K., Warner, D.L., Zhang, Z., Vargas, R., 2019. Methane emissions from tree stems: a new frontier in the global carbon cycle. N. Phytol. 222, 18–28.

Bartlett, K.B., Crill, P.M., Sebacher, D.I., Harriss, R.C., Wilson, J.O., Melack, J.M., 1988. Methane flux from the central Amazonian floodplain. J. Geophys. Res 93, 1574–1582.

Basso, L.S., Marani, L., Gatti, L.V., Miller, J.B., Gloor, M., Melack, J., et al., 2021. Amazon methane budget derived from multi-year airborne observations highlights regional variations in emissions. Comm. Earth Environ. 2, 246. https://doi.org/10.1038/s43247-021-00314-4.

Bastviken, D., Treat, C.C., Pangala, S.R., Gauci, V., Enrich-Prast, A., Karlson, M., Gålfalk, M., Romano, M.B., Sawakuchi, H.O., 2022. The importance of plants for methane emission at the ecosystem scale. Aquat. Bot. (in this issue).

Bazzi, H., Baghdadi, N., El Hajj, M., Zribi, M., Minh, D.H.T., Ndikumana, E., Courault, D., Belhouchette, H., 2019. Mapping paddy rice using Sentinel-1 SAR time series in Camargue, France. Remote Sens 11, 887.

Beland, M., Parker, G., Sparrow, B., Harding, D., Chasmer, L., Phinn, S., Antonarakis, A., Strahler, A., 2019. On promoting the use of lidar systems in forest ecosystem research. For. Ecol. Manag. 450, 117484.

Belger, L., Forsberg, B.R., Melack, J.M., 2011. Factors influencing carbon dioxide and methane emissions from interfluvial wetlands of the upper Negro River basin, Brazil. Biogeochemistry 105, 171–183.

Betbeder, J., Gond, V., Frappart, F., Baghdadi, N.N., Briant, G., Bartholomé, E., 2013. Mapping of Central Africa forested wetlands using remote sensing. IEEE J. Sel. Topics Appl. Earth Obs. Remote Sens 7, 531–542.

Bhatnagar, S., Gill, L., Regan, S., Waldren, S., Ghosh, B., 2021. A nested drone-satellite approach to monitoring the ecological conditions of wetlands. ISPRS J. Photogramm. Remote Sens. 174, 151–165.

Bloom, A.A., Bowman, K.W., Lee, M., Turner, A.J., Schroeder, R., Worden, J.R., et al., 2017. A global wetland methane emissions and uncertainty dataset for atmospheric chemical transport models (WetCHARTs version 1.0). Geosci. Model Dev. 10, 2141–2156.

Bodmer, P., Vroom, R., Stepina, T., del Giorgio, P., Kosten, S., 2022. Methane fluxes of vegetated areas in natural freshwater ecosystems: Assessments and global significance. EarthArXiv. ⟨https://eartharxiv.org/repository/view/2904/⟩.

Bontemps, S., Defourny, P., van Bogaert, E., Arino, O., Kalagirou, V., Ramos Peres, J., 2011. Globcover products description and validation report. Technical report, ESA. URL: ⟨epic.awi.de/id/eprint/31014/16/GLOBCOVER2009_284.Validation_Report_2–2.pdf.285⟩.

Borah, S.B., Sivasankar, T., Ramya, M., Raju, P., 2018. Flood inundation mapping and monitoring in Kaziranga National Park, Assam using Sentinel-1 SAR data. Environ. Monit. Assess. 190, 1–11.

Bourgeau-Chavez, L., Endres, S., Battaglia, M., Miller, M.E., Banda, E., Laubach, Z., Higman, P., Chow Fraser, P., Marcaccio, J., 2015. Development of a bi-national Great Lakes coastal wetland and land use map using three-season PALSAR and Landsat imagery. Remote Sens 7, 8655–8682.

Bridgham, S.D., Cadillo-Quiroz, H., Keller, J.K., Zhuang, Q.L., 2013. CH_4 emissions from wetlands: biogeochemical, microbial, and modeling perspectives from local to global scales. Glob. Change Biol. 19, 1325–1346.

Brock, J.C., Wright, C.W., Sallenger, A.H., Krabill, W.B., Swift, R.N., 2002. Basis and methods of NASA airborne topographic mapper lidar surveys for coastal studies. J. Coast. Res 18, 1–13.

Buchhorn, M., Lesiv, M., Tsendbazar, N.-E., Herold, M., Bertels, L., Smets, B., 2020. Copernicus global land cover layers—collection 2. Remote Sensing 12, 1044.

Buckingham, R., Staenz, K., 2008. Review of current and planned civilian space hyperspectral sensors for EO. S187-S197 Can. J. Remote Sens. 34. https://doi.org/10.5589/m08-002.

Bwangoy, J.-R.B., Hansen, M.C., Roy, D.P., De Grandi, G., Justice, C.O., 2010. Wetland mapping in the Congo Basin using optical and radar remotely sensed data and derived topographical indices. Remote Sens. Environ. 114, 73–86.

Campbell, A.D., Fatoyinbo, T., Charles, S.P., Bourgeau-Chavez, L.L., Goes, J., Gomes, H., Halabisky, M., Holmquist, J., Lohrenz, S., Mitchell, C., Moskal, L.M., Poulter, B., Qiu, H., De Sousa, C.H.R., Sayers, M., Simard, M., Stewart, A.J., Singh, D., Trettin, C., Wu, J., Zhang, X., Lagomasino, D., 2022. A review of carbon monitoring in wet carbon systems using remote sensing. Environ. Res. Lett. 17, 025009 https://doi.org/10.1088/1748-9326/ac4d4d.

Canisius, F., Brisco, B., Murnaghan, K., Van Der Kooij, M., Keizer, E., 2019. SAR backscatter and InSAR coherence for monitoring wetland extent, flood pulse and vegetation: A study of the Amazon lowland. Remote Sens 11, 720. https://doi.org/10.3390/rs11060720.

Chapman, B.D., Russo, I.M., Galdi, C., Morris, M., Di Bisceglie, M., Zuffada, C., Downs, B., Lavalle, M., Loria, E., O'Brien, A., 2022. Comparison of SAR and CYGNSS surface water extent metrics. IEEE J. Sel. Top. Appl. Earth Obs. Remote Sens. 15, 3235–3245.

Chen, Z., White, L., Banks, S., Behnamian, A., Montpetit, B., Pasher, J., Duffe, J., Bernard, D., 2020. Characterizing marsh wetlands in the Great Lakes Basin with C-band InSAR observations. Remote Sens. Environ. 242, 111750.

Ramsar Convention on Wetlands, 2018. Global Wetland Outlook: State of the World's Wetlands and their Services to People. Ramsar Convention Secretariat, Gland, Switzerland.

Clark, D.B., Mercado, L.M., Sitch, S., Jones, C.D., Gedney, N., Best, M.J., et al., 2011. The Joint UK Land Environment Simulator (JULES), model description–Part 2: carbon fluxes and vegetation dynamics. Geosci. Model Dev. 4, 701–722.

Clewley, D., Whitcomb, J., Moghaddam, M., McDonald, K., Chapman, B., Bunting, P., 2015. Evaluation of ALOS PALSAR data for high-resolution mapping of vegetated wetlands in Alaska. Remote Sens 7, 7272–7297. https://doi.org/10.3390/rs70607272.

Covey, K.R., Megonigal, J.P., 2019. Methane Production and Emissions in Trees and forests. N. Phytol. 222, 35–51.

Cowardin, L.M., Carter, V., Golet, F.C., LaRoe, E.T., 1979. Classification of Wetlands and Deepwater Habitats of the United States. U.S. Fish and Wildlife Service, Office of Biological Services, Washington, DC, USA.

Dacey, J.W.H., 1981. Pressurized ventilation in the yellow waterlily. Ecology 62, 1137–1147.

Dahl, T.E., 2011. Status and Trends of Wetlands in the Conterminous United States 2004 to 2009. US Department of the Interior, US Fish and Wildlife Service, Fisheries and Habitat Conservation, Washington DC, USA.

Davidson, N.C., Fluet-Chouinard, E., Finlayson, C.M., 2018. Global extent and distribution of wetlands: trends and issues. Mar. Freshw. Res 69, 620–627. https://doi.org/10.1071/MF17019.

Davidson, S.J., Sloan, V.L., Phoenix, G.K., Wagner, R., Fisher, J.P., Oechel, W.C., Zona, D., 2016a. Vegetation type dominates the spatial variability in CH_4 emissions across multiple Arctic tundra landscapes. Ecosystems 19, 1116–1132.

Davidson, S.J., Santos, M.J., Sloan, V.L., Watts, J.D., Phoenix, G.K., Oechel, W.C., Zona, D., 2016b. Mapping arctic tundra vegetation communities using field spectroscopy and multispectral satellite data in north Alaska, USA. Remote Sens. 8, 978. https://doi.org/10.3390/rs8120978.

Delwiche, K.B., Knox, S.H., Malhotra, A., Fluet-Chouinard, E., McNicol1, G., Feron, S., et al., 2021. FLUXNET- CH4: A global, multi-ecosystem dataset and analysis of methane seasonality from freshwater wetlands. Earth Syst. Sci. Data Disc. https://doi.org/10.5194/essd-2020-307.

Di Vittorio, C.A., Georgakakos, A.P., 2018. Land cover classification and wetland inundation mapping using MODIS. Remote Sens. Environ. 204, 1–17.

Dlugokencky, E.J. 2021. Trends in atmospheric methane. ⟨www.esrl.noaa.gov/gmd/ccgg/trends_ch4/⟩.

Draper, F.C., Roucoux, K.H., Lawson, I.T., Mitchard, E.T.A., Honorio Coronado, E.N., Lähteenoja, O., et al., 2014. The distribution and amount of carbon in the largest peatland complex in Amazonia. Environ. Res. Lett. 9 https://doi.org/10.1088/1748-9326/9/12/124017.

Dronova, I., Gong, P., Wang, L., Zhong, L., 2015. Mapping dynamic cover types in a large seasonally flooded wetland using extended principal component analysis and object-based classification. Remote Sens. Environ. 158, 193–206.
Dronova, I., Gong, P., Clinton, N.E., Wang, L., Fu, W., Qi, S., Liu, Y., 2012. Landscape analysis of wetland plant functional types: The effects of image segmentation scale, vegetation classes and classification methods. Remote Sens. Environ. 127, 357–369.
Engle, D.L., Melack, J.M., Doyle, R.D., Fisher, T.R., 2008. High rates of net primary productivity and turnover for floating grasses on the Amazon floodplain: Implications for aquatic respiration and regional CO_2 flux. Glob. Change Biol. 14, 369–381.
Evans, T.L., Costa, M., Tomas, W.M., Camilo, A.R., 2014. Large-scale habitat mapping of the Brazilian Pantanal wetland: a synthetic aperture radar approach. Remote Sens. Environ. 155, 89–108.
Fassoni-Andrade, A.C., Paiva, R.C.D., Rudorff, C.M., Barbosa, C.C.F., Novo, E.M.L.M., 2020. High-resolution mapping of floodplain topography from space: a case study in the Amazon. Remote Sens. Environ. 251, 112065 https://doi.org/10.1016/j.rse.2020.112065.
Fassoni-Andrade, A.C., Fleischmann, A.S., Papa, F., Paiva, R.C.D., Wongchuig, S., Melack, J.M., Moreira, A.A., Paris, A., Ruhoff, A., Barbosa, C., Andrade Macie, D., Novo, E., Durand, F., Frappart, F., Aires, F., Abrahão, G.M., Ferreira-Ferreira, J., Espinoza, J.C., Laipelt, L., Costa, M.H., Espinoza-Villar, R., Calmant, S., Pellet, V., 2021. Amazon hydrology from space: scientific advances and future challenges. e2020RG000728 Rev. Geophys. 59. https://doi.org/10.1029/2020RG000728.
Fatoyinbo, T.E., Simard, M., 2013. Height and biomass of mangroves in Africa from ICESat/GLAS and SRTM. Intern. J. Remote Sens. 34, 668–681.
Ferreira-Ferreira, J., Silva, T.S.F., Streher, A.S., Affonso, A.G., de Almeida Furtado, L.F., Forsberg, B.R., et al., 2015. Combining ALOS/PALSAR derived vegetation structure and inundation patterns to characterize major vegetation types in the Mamirauá Sustainable Development Reserve, Central Amazon floodplain, Brazil. Wetl. Ecol. Manag. 23, 41–59. https://doi.org/10.1007/s11273-014-9359-1.
Fleischmann, A.S., Papa, F., Fassoni-Andrade, A., Melack, J.M., Wongchuig, S., Paiva, R. C.D., et al., 2022. How much inundation occurs in the Amazon River basin? Remote Sens. Environ. 278, 113099 https://doi.org/10.1016/j.rse.2022.113099.
Fluet-Chouinard, E., Lehner, B., Rebelo, L.M., Papa, F., Hamilton, S.K., 2015. Development of a global inundation map at high spatial resolution from topographic downscaling of coarse-scale remote sensing data. Remote Sens. Environ. 158, 348–361. https://doi.org/10.1016/j.rse.2014.10.015.
Fonseca, L.D.M., Dalagnol, R., Malhi, Y., Rifai, S.W., Costa, G.B., Silva, T.S.F., Da Rocha, H.R., Tavares, I.B., Borma, L.S., 2019. Phenology and seasonal ecosystem productivity in an Amazonian floodplain forest. Remote Sens 11, 1530.
Furtado, L.F.A., Silva, T.S.F., Novo, E.M.L.M., 2016. Dual-season and full-polarimetric C band SAR assessment for vegetation mapping in the Amazon várzea wetlands. Remote Sens. Environ. 174, 212–222. https://doi.org/10.1016/j.rse.2015.12.013.
Gallant, A.L., 2015. The challenges of remote monitoring of wetlands. Remote Sens 7, 10938–10950. https://doi.org/10.3390/RS70810938.
Gash, J., Keller, M., Silva-Dias, P. (Eds.), 2009. Amazonia and Global Change. American Geophysical Union.
Gašparović, M., Klobučar, D., 2021. Mapping floods in lowland forest using Sentinel-1 and Sentinel-2 data and an object-based approach. Forests 12, 553.
Gloor, M., Gatti, L.V., Wilson, C., Parker, R.J., Boesch, H., Popa, E., et al., 2021. Large methane emissions from the Pantanal during rising water-levels revealed by regularly measured lower troposphere CH_4 profiles. e2021GB006964 Glob. Biogeochem. Cycles 35. https://doi.org/10.1029/2021GB006964.
Gomes, V.C., Queiroz, G.R., Ferreira, K.R., 2020. An overview of platforms for big earth observation data management and analysis. Remote Sens 12, 1253.
Gumbricht, T., Roman-Cuesta, R.M., Verchot, L., Herold, M., Wittmann, F., Householder, E., Herold, N., Murdiyarso, D., 2017. An expert system model for mapping tropical wetlands and peatlands reveals South America as the largest contributor. Glob. Change Biol. 23, 3581–3599. https://doi.org/10.1111/gcb.13689.
Hamilton, S.K., Sippel, S.J., Melack, J.M., 1995. Oxygen depletion and carbon dioxide and methane production in waters of the Pantanal wetland of Brazil. Biogeochemistry 30, 115–141. https://doi.org/10.1007/BF00002727.
Hamilton, S.K., Sippel, S.J., Melack, J.M., 2002. Comparison of inundation patterns among major South American floodplains. J. Geophys. Res. 107. D20 1029/2000JD000306.
Hamilton, S.K., Sippel, S.J., Melack, J.M., 2004. Seasonal inundation patterns in two large savanna floodplains of South America: the Llanos de Moxos (Bolivia) and the Llanos del Orinoco (Venezuela and Colombia). Hydrol. Process. 18, 2103–2116.
Hamilton, S.K., Sippel, S.J., Chanton, J.P., Melack, J.M., 2014. Plant-mediated transport and isotopic composition of methane from shallow tropical wetlands. Inland Waters 4, 369–376. https://doi.org/10.5268/IW-4.4.734.
Hawes, J.E., Peres, C.A., Riley, L.B., Hess, L.L., 2012. Landscape-scale variation in structure and biomass of Amazonian seasonally flooded and unflooded forests. For. Ecol. Manag. 281, 163–176.
Hawker, L., Uhe, P., Paulo, L., Sosa, J., Savage, J., Sampson, C., Neal, J., 2022. A 30 m global map of elevation with forests and buildings removed. Environ. Res. Lett. 17, 024016.
Hess, L.L., Melack, J.M., 2003. Remote sensing of vegetation and flooding on Magela Creek floodplain (Northern Territory, Australia) with SIR-C synthetic aperture radar. Hydrobiologia 500, 65–82.
Hess, L.L., Melack, J.M., Simonett, D., 1990. Radar detection of flooding beneath the forest canopy: a review. Int. J. Remote Sens. 11, 1313–1325.
Hess, L.L., Melack, J.M., Filoso, S., Wang, Y., 1995. Delineation of inundated area and vegetation along the Amazon floodplain with the SIR-C synthetic aperture radar. IEEE Trans. Geosci. Remote Sens. 33, 896–904.
Hess, L.L., Melack, J.M., Novo, E.M.L.M., Barbosa, C.C.F., Gastil, M., 2003. Dual-season mapping of wetland inundation and vegetation for the central Amazon basin. Remote Sens. Environ. 87, 404–428.
Hess, L.L., Novo, E.M.L.M., Slaymaker, D.M., Holt, J., Steffen, C., Valeriano, D.M., et al., 2002. Geocoded digital videography for validation of land cover mapping in the Amazon basin. Int. J. Remote Sens. 7, 1527–1556.
Hess, L.L., Melack, J.M., Affonso, A.G., Barbosa, C., Gastil, M., Novo, E.M.L.M., 2015. Amazonian wetlands: extent, vegetative cover, and dual season inundation area. Wetlands 35, 745–756.
Hondula, K.L., DeVries, B., Jones, C.N., Palmer, M.A., 2021. Effects of using high resolution satellite-based inundation time series to estimate methane fluxes from forested wetlands. Geophys. Res. Lett. 48 e2021GL092556.
Hosseiny, B., Mahdianpari, M., Brisco, B., Mohammadimanesh, F., Salehi, B., 2021. WetNet: a spatial–temporal ensemble deep learning model for wetland classification using Sentinel-1 and Sentinel-2. IEEE Trans. Geosci. Remote Sens 60, 3113856. https://doi.org/10.1109/TGRS.2021.3113856.
Hoyt, A.M., Chaussard, E., Seppalainen, S.S., Harvey, C.F., 2020. Widespread subsidence and carbon emissions across Southeast Asian peatlands. Nat. Geosci. 13, 435–440.
Hu, Q., Cai, J., Yao, B., Wu, Q., Wang, Y., Xu, X., 2016. Plant-mediated methane and nitrous oxide fluxes from a carex meadow in Poyang Lake during drawdown periods. Plant Soil 400, 367–380.
Hugelius, G., Tarnocai, C., Broll, G., Canadell, J.G., Kuhry, P., Swanson, D.K., 2013. The Northern Circumpolar Soil Carbon Database: spatially distributed datasets of soil coverage and soil carbon storage in the northern permafrost regions, Earth Syst. Sci. Data 5, 3–13. https://doi.org/10.5194/essd-5-3-2013.
Hutchinson, G.E., 1975. A Treatise on Limnology. Vol III – Limnological Botany. John Wiley & Sons, Inc, New York.
Jensen, K., McDonald, K., 2019. Surface water microwave product series version 3: a near-real time and 25-year historical global inundated area fraction time series from active and passive microwave remote sensing. IEEE Geosci. Remote Sens. Lett. 16, 1402–1406. https://doi.org/10.1109/lgrs.2019.2898779.
Jensen, K., McDonald, K., Podest, E., Rodriguez-Alvarez, N., Horna, V., Steiner, N., 2018. Assessing L-band GNSS-reflectometry and imaging radar for detecting sub-canopy inundation dynamics in a tropical wetlands complex. Remote Sens 10, 1431.
Junk, W.J., Piedade, M.T.F., 1997. Plant life in the floodplain with special reference to herbaceous plants. Ecological Studies 126. In: Junk, W.J. (Ed.), Central Amazon Floodplain: Ecology of a Pulsing System. Springer, pp. 17–185.
Junk, W.J., Piedade, M.T.F., Schöngart, J., Cohn-Haft, M., Adeney, J.M., Wittmann, F., 2011. A classification of major naturally-occurring Amazonian lowland wetlands. Wetlands 31, 623–640.
Karlson, M., Galfalk, M., Crill, P., Bousquet, P., Saunois, M., Bastviken, D., 2019. Delineating northern peatlands using Sentinel-1 time series and terrain indices from local and regional digital elevation models. Remote Sens. Environ. 21, 111252.
Kasischke, E.S., Melack, J.M., Dodson, M.C., 1997. The use of imaging radar for ecological applications-a review. Remote Sens. Environ. 59, 141–156.
Kitambo, B., Papa, F., Paris, A., Tshimanga, R.M., Calmant, S., Fleischmann, A.S., Frappart, F., Becker, M., Tourian, M.J., Prigent, C., 2022. A combined use of in situ and satellite-derived observations to characterize surface hydrology and its variability in the Congo River Basin. Hydrol. Earth Syst. Sci. 26, 1857–1882.
Klemas, V., 2013. Remote sensing of emergent and submerged wetlands: an overview. Intern. J. Remote Sens 34, 6286–6320.
Knox, S.H., Bansal, S., McNicol, G., Schafer, K., Sturtevant, C., Ueyama, M., et al., 2021. Identifying dominant environmental predictors of freshwater wetland methane fluxes across diurnal to seasonal time scales. Glob. Change Biol. 27, 3582–3604. https://doi.org/10.1111/gcb.15661.
Kokaly, R.F., Asner, G.P., Ollinger, S.V., Martin, M.E., Wessman, C.A., 2009. Characterizing canopy biochemistry from imaging spectroscopy and its application to ecosystem studies. Remote Sens. Environ. 113, S78–S91.
Kuhn, M.A., Varner, R.K., Bastviken, D., Crill, P.M., MacIntyre, S., Turetsky, M., Walter Anthony, K., McGuire, A.D., Olefeldt, D., 2021. BAWLD-CH_4: a comprehensive database of methane fluxes from boreal and Arctic wetlands and lakes. Earth Syst. Sci. Data. https://doi.org/10.5194/essd-2021-141.
Laborte, A.G., Gutierrez, M.A., Balanza, J.G., Saito, K., Zwart, S.J., Boschetti, M., Murty, M., Villano, L., Aunario, J.K., Reinke, R., 2017. RiceAtlas, a spatial database of global rice calendars and production. Sci. Data 4, 1–10.
LaCapra, V., Melack, J.M., Gastil, M., Valeriano, D., 1996. Remote sensing of foliar chemistry of inundated rice with imaging spectrometry. Remote Sens. Environ. 55, 50–58.
Le Mer, J., Roger, P., 2001. Production, oxidation, emission and consumption of methane by soils: a review. Eur. J. Soil Biol. 37, 25–50.
Lee, H., Yuan, Y., Jung, H.C., Beighley, E., 2015. Mapping wetland water depths over the central Congo Basin using PALSAR ScanSAR, Envisat altimetry, and MODIS VCF data. Remote Sens. Environ. 159, 70–79.
Lee, H., Beighley, R.E., Alsdorf, D., Jung, H.C., Shum, C., Duan, J., Guo, J., Yamazaki, D., Andreadis, K., 2011. Characterization of terrestrial water dynamics in the Congo Basin using GRACE and satellite radar altimetry. Remote Sens. Environ. 115, 3530–3538.
Lehner, B., Döll, P., 2004. Development and validation of a global database of lakes, reservoirs and wetlands. J. Hydrol. 296, 1–22. https://doi.org/10.1016/j.jhydrol.2004.03.028.
Lesiv, M., See, L., Laso Bayas, J.C., Sturn, T., Schepaschenko, D., Karner, M., Moorthy, I., McCallum, I., Fritz, S., 2018. Characterizing the spatial and temporal availability of very high resolution satellite imagery in Google Earth and Microsoft Bing maps as a source of reference data. Land 7, 118.

Liao, H., Wdowinski, S., Li, S., 2020. Regional-scale hydrological monitoring of wetlands with Sentinel-1 InSAR observations: case study of the South Florida Everglades. Remote Sens. Environ. 251, 112051.
Liu, L., Zhuang, Q., Oh, Y., Shurpali, N.J., Kim, S., Poulter, B., 2020. Uncertainty quantification of global net methane emissions from terrestrial ecosystems using a mechanistically based biogeochemistry model. e2019JG005428 J. Geophys. Res. Biogeosci. 125. https://doi.org/10.1029/2019JG005428.
Liu, L., Zhang, X., Gao, Y., Chen, X., Shuai, X., Mi, J., 2021. Finer-resolution mapping of global land cover: Recent developments, consistency analysis, and prospects. J. Remote Sens 2021, 528997. https://doi.org/10.34133/2021/5289697.
Lucas, R., Rebelo, L.-M., Fatoyinbo, L., Rosenqvist, A., Itoh, T., Shimada, M., Simard, M., Souza-Filho, P.W., Thomas, N., Trettin, C., Accad, A., Carreiras, J., Hilarides, L., 2014. Contribution of L-band SAR to systematic global mangrove monitoring. Mar. Freshw. Res. 65, 589–603. https://doi.org/10.1071/MF13177.
Maciel, D.A., Novo, E.M.D.M., Barbosa, C.C.F., Martins, V.S., Flores Júnior, R., Oliveira, A.H., Sander De Carvalho, L.A., Lobo, F.D.L., 2020. Evaluating the potential of CubeSats for remote sensing reflectance retrieval over inland waters. Intern. J. Remote Sens 41, 2807–2817.
Mahdavi, S., Salehi, B., Granger, J., Amani, M., Brisco, B., Huang, W., 2018. Remote sensing for wetland classification: a comprehensive review. GIScience Remote Sens 55, 623–658.
Mahdianpari, M., Brisco, B., Granger, J., Mohammadimanesh, F., Salehi, B., Homayouni, S., Bourgeau-Chavez, L., 2021. The third generation of pan-Canadian wetland map at 10 m resolution using multisource earth observation data on cloud computing platform. IEEE J. Sel. Top. Appl. Earth Obs. Remote Sens 14, 8789–8803.
Mahdianpari, M., Jafarzadeh, H., Granger, J.E., Mohammadimanesh, F., Brisco, B., Salehi, B., Homayouni, S., Weng, Q., 2020a. A large-scale change monitoring of wetlands using time series Landsat imagery on Google Earth Engine: a case study in Newfoundland. GISci. Remote Sens. 57, 1102–1124.
Mahdianpari, M., Salehi, B., Mohammadimanesh, F., Brisco, B., Homayouni, S., Gill, E., DeLancey, E.R., Bourgeau-Chavez, L., 2020b. Big data for a big country: the first generation of Canadian wetland inventory map at a spatial resolution of 10-m using Sentinel-1 and Sentinel-2 data on the Google Earth Engine cloud computing platform. Can. J. Remote Sens. 46, 15–33.
Mahdianpari, M., Brisco, B., Granger, J.E., Mohammadimanesh, F., Salehi, B., Banks, S., Homayouni, S., Bourgeau-Chavez, L., Weng, Q., 2020c. The second generation Canadian wetland inventory map at 10 meter resolution using Google Earth Engine. Can. J. Remote Sens. 46, 360–375. https://doi.org/10.1080/07038992.2020.1802584.
Mandlburger, G., 2020. A Review of Airborne Laser Bathymetry for Mapping of Inland and Coastal Waters. Hydrographische Nachrichten 116. Deutsche Hydrographische Gesellschaft 6-15, Rostock doi.org/10.23784/HN116-01.
Marani, L., Alvala, P.C., 2007. Methane emissions from lakes and floodplains in Pantanal, Brazil. Atmos. Environ. 41, 1627–1633.
Margono, B.A., Bwangoy, J.-R.B., Potapov, P.V., Hansen, M.C., 2014. Mapping wetlands in Indonesia using Landsat and PALSAR data-sets and derived topographical indices. Geo-Spat. Inf. Sci. 17, 60–71. https://doi.org/10.1080/10095020.2014.898560.
Mateo-Garcia, G., Veitch-Michaelis, J., Smith, L., Oprea, S.V., Schumann, G., Gal, Y., Baydin, A.G., Backes, D., 2021. Towards global flood mapping onboard low cost satellites with machine learning. Sci. Rep. 11, 1–12.
McCabe, M.F., Rodell, M., Alsdorf, D.E., Miralles, D.G., Uijlenhoet, R., Wagner, W., Lucieer, A., Houborg, R., Verhoest, N.E., Franz, T.E., 2017. The future of Earth observation in hydrology. Hydrol. Earth Syst. Sci. 21, 3879–3914.
Melack, J.M., 2004. Remote sensing of tropical wetlands (Remote Sensing for Natural Resources Management and Environmental Monitoring). In: Ustin, S. (Ed.), Manual of Remote Sensing, 3rd ed.,, 4. John Wiley & Sons, pp. 319–343.
Melack, J.M., Hess, L.L., 2010. Remote sensing of the distribution and extent of wetlands in the Amazon basin. In: Junk, W.J., Piedade, M., Wittmann, F., Schöngart, J., Parolin, P. (Eds.), Amazonian Floodplain Forests: Ecophysiology, Ecology, Biodiversity and Sustainable Management. Ecological Studies 210. Springer, pp. 43–59.
Melack, J.M., Basso, L.S., Fleischmann, A.S., Botía, S., Guo, M., Zhou, W., Barbosa, P.M., Amaral, J.H.F., MacIntyre, S., 2022. Challenges regionalizing methane emissions using aquatic environments in the Amazon basin as examples. Front. Environ. Sci. 10, 866082 https://doi.org/10.3389/fenvs.2022.866082.
Melton, J.R., Wania, R., Hodson, E.L., Poulter, B., Ringeval, B., Spahni, R., et al., 2013. Present state of global wetland extent and wetland methane modelling: conclusions from a model inter-comparison project (WETCHIMP). Biogeosciences 10, 753–788.
Mitsch, W.J., Gosselink, J.G., 2000. Wetlands. John Wiley & Sons, Inc, New York.
Montgomery, J., Mahoney, C., Brisco, B., Boychuk, L., Cobbaert, D., Hopkinson, C., 2021. Remote sensing of wetlands in the prairie pothole region of North America. Remote Sens 13, 3878.
Morris, M., Chew, C., Reager, J.T., Shah, R., Zuffada, C., 2019. A novel approach to monitoring wetland dynamics using CYGNSS: everglades case study. Remote Sens. Environ. 233, 111417.
Murray, N.J., Worthington, T.A., Bunting, P., Duce, S., Hagger, V., Lovelock, C.E., Lucas, R., Saunders, M.I., Sheaves, M., Spalding, M., Waltham, N.J., Lyons, M.B., 2022. High-resolution mapping of losses and gains of Earth's tidal wetlands. Science 376, 744–749.
Nardi, F., Annis, A., Baldassarre, G.D., Vivoni, E.R., Grimaldi, S., 2019. GFPLAIN250m, a global high-resolution dataset of Earth's floodplains. Sci. Data 6, 180309. https://doi.org/10.1038/sdata.2018.309.
Niculescu, S., Boissonnat, J.-B., Lardeux, C., Roberts, D., Hanganu, J., Billey, A., Constantinescu, A., Doroftei, M., 2020. Synergy of high-resolution radar and optical images satellite for identification and mapping of wetland macrophytes on the Danube Delta. Remote Sens 12, 2188. https://doi.org/10.3390/rs12142188.
Novo, E.M.L.M., Filho, W.P., Melack, J.M., 2013. LBA-ECO LC-07 Reflectance Spectra and Water Quality of Amazon Basin Floodplain Lakes. ORNL DAAC, Oak Ridge, Tennessee, USA https://doi.org/10.3334/ORNLDAAC/1144.
Olefeldt, D., Hovemyr, M., Kuhn, M.A., Bastviken, D., Bohn, T.J., Connolly, J., Crill, P., et al., 2021. The boreal–arctic wetland and lake dataset (BAWLD). Earth Syst. Sci. Data 13, 5127–5149.
Oliveira Junior, E.S., van Bergen, T.J.H.M., Nauta, J., Budiša, A., Aben, R.C.H., Weideveld, S.T.J., et al., 2020. Water hyacinth's effect on greenhouse gas fluxes: a field study in a wide variety of tropical water bodies. Ecosystems. https://doi.org/10.1007/s10021-020-00564-x.
Palace, M., Herrick, C., DelGreco, J., Finnell, D., Garnello, A.J., McCalley, C., McArthur, K., Sullivan, F., Varner, R.K., 2018. Determining subarctic peatland vegetation using an unmanned aerial system (UAS). Remote Sens. 10, 1498. https://doi.org/10.3390/rs10091498.
Pangala, S.R., Enrich-Prast, A., Basso, L.S., Peixoto, R.B., Bastviken, D., Hornibrook, E.R. C., et al., 2017. Large emissions from floodplain trees close the Amazon methane budget. Nature 552, 230–234. https://doi.org/10.1038/nature24639.
Papa, F., Prigent, C., Jimenez, C., Aires, F., Rossow, W.B., 2010. Interannual variability of surface water extent at global scale, 1993-2004. J. Geophys. Res 115, D12111. https://doi.org/10.1029/2009JD012674.
Parrens, M., Al Bitar, A., Frappart, F., Paiva, R., Wongchuig, S., Papa, F., Yamasaki, D., Kerr, Y., 2019. High resolution mapping of inundation area in the Amazon basin from a combination of L-band passive microwave, optical and radar datasets. Int. J. Appl. Earth Obs. Geoinf. 81, 58–71. https://doi.org/10.1016/j.jag.2019.04.011.
Peixoto, R.B., Machado-Silva, F., Marotta, H., et al., 2015. Spatial versus day-to-day within-lake variability in tropical floodplain lake CH_4 emissions – developing optimized approaches to representative flux measurements. e0123319 PLoS One 10. https://doi.org/10.1371/journal.pone.0123319.
Pereira, L.O., Furtado, L.F.A., Novo, E.M.L.M., Sant'Anna, S.J.S., Liesenberg, V., Silva, T. S.F., 2018. Multifrequency and full-polarimetric SAR assessment for estimating above ground biomass and leaf area index in the Amazon várzea wetlands. Remote Sens 10, 1355. https://doi.org/10.3390/rs10091355.
Perennou, C., Guelmami, A., Paganini, M., Philipson, P., Poulin, B., Strauch, A., Tottrup, C., Truckenbrodt, J., Geijzendorffe, I.R., 2018. Mapping Mediterranean wetlands with remote sensing: A good-looking map is not always a good map. Adv. Ecol. Res. 58, 243–277. https://doi.org/10.1016/bs.aecr.2017.12.002.
Potapov, P., Li, X., Hernandez-Serna, A., Tyukavina, A., Hansen, M.C., Kommareddy, A., Pickens, A., Turubanova, S., Tang, H., Silva, C.E., 2020. Mapping global forest canopy height through integration of GEDI and Landsat data. Remote Sens. Environ. 253, 112165 https://doi.org/10.1016/j.rse.2020.112165.
Potter, C.S., 1997. An ecosystem simulation model for methane production and emission from wetlands. Glob. Biogeochem. Cycles 11, 495–506.
Potter, C.S., Melack, J.M., Engle, D., 2014. Modeling carbon dynamics and methane emissions from Amazon floodplain ecosystems. Wetlands 34, 501–511.
Prigent, C., Jimenez, C., Bousquet, P., 2020. Satellite-derived global surface water extent and dynamics over the last 25 years (GIEMS-2). J. Geophys. Res: Atm. 125 e2019JD030711.
Prigent, C., Papa, F., Aires, F., Rossow, W.B., Matthews, E., 2007. Global inundation dynamics inferred from multiple satellite observations, 1993-2000. D12107 J. Geophys. Res. 112. https://doi.org/10.1029/2006JD007847.
Radomsky, P., Holbrook, B.V., 2015. A comparison of two hydroacoustic methods for estimating submerged macrophyte distribution and abundance: A cautionary note. J. Aquat. Plant Manag. 53, 151–159.
Rapinel, S., Mony, C., Lecoq, L., Clement, B., Thomas, A., Hubert-Moy, L., 2019. Evaluation of Sentinel-2 time-series for mapping floodplain grassland plant communities. Remote Sens. Environ. 223, 115–129.
Resop, J.P., Lehmann, L., Hession, W.C., 2019. Drone laser scanning for modeling riverscape topography and vegetation: Comparison with traditional aerial Lldar. Drones 3, 35.
Riley, W.J., Subin, Z.M., Lawrence, D.M., Swenson, S.C., Torn, M.S., Meng, L., et al., 2011. Barriers to predicting changes in global terrestrial methane fluxes: analyses using CLM4Me, a methane biogeochemistry model integrated in CESM. Biogeosci. Disc 8, 1733–1807.
Ringeval, B., Houweling, S., van Bodegom, P.M., Spahni, R., van Beek, R., Joos, F., et al., 2014. Methane emissions from floodplains in the Amazon Basin: challenges in developing a process-based model for global applications. Biogeosciences 11, 1519–1558. https://doi.org/10.5194/bg-11-1519-2014.
Rosentreter, J.A., Borges, A.V., Deemer, B.R., Holgerson, M.A., Liu, S., Song, C., Melack, J.M., Raymond, P.A., Duarte, C.M., Allen, G.H., Olefeldt, D., Poulter, B., Battin, T.I., Eyre, B.D., 2021. Half of global methane emissions come from highly variable aquatic ecosystem sources. Nat. Geosci. 14, 225–230. https://doi.org/10.1038/S41561-021-00715-2.
Sadro, S., Gastil-Buhl, M., Melack, J.M., 2007. Characterizing patterns of plant distribution in a southern California salt marsh using topographic and hyperspectral data and local tidal hydrodynamics. Remote Sens. Environ. 110, 226–239.
Sahagian, D., Melack, J.M. (eds.). (1998). Global Wetland Distribution and Functional Characterization: Trace Gases and the Hydrologic Cycle. IGBP Report 46.
Santos, M.J., Khanna, S., Hestir, E.L., Greenberg, J.A., Ustin, S.L., 2016. Measuring landscape-scale spread and persistence of an invaded submerged plant community from airborne remote sensing. Ecol. Appl. 26, 1733–1744.
Sartori, L.R., Imai, N.N., Mura, J.C., Novo, E.M.L.M., Silva, T.S.F., 2011. Mapping macrophyte species in the Amazon floodplain wetlands using fully polarimetric ALOS/PALSAR data. IEEE Trans. Geosci. Remote Sens. 49, 4717–4728.
Saunois, M., Stavert, A.R., Poulter, B., Bousquet, P., Canadell, J.G., Jackson, R.B., et al., 2020. The global methane budget: 2000-2017. Earth Syst. Sci. Data 12, 1561–1623. https://doi.org/10.5194/essd-12-1561-2020.

Schlaffer, S., Chini, M., Dorigo, W., Plank, S., 2022. Monitoring surface water dynamics in the prairie pothole region of North Dakota using dual-polarised Sentinel-1 synthetic aperture radar (SAR) time series. Hydrol. Earth Syst. Sci. 26, 841–860.
Schlesinger, W.H., Bernhardt, E.S., 2013. Biogeochemistry. Elsevier, Amsterdam.
Schroeder, R., McDonald, K.C., Chapman, B.D., Jensen, K., Podest, E., Tessler, Z.D., et al., 2015. Development and evaluation of a multi-year fractional surface water data set derived from active/passive microwave remote sensing data. Remote Sens 7, 16688–16732. https://doi.org/10.3390/rs71215843.
Sculthorpe, C.D., 1967. The Biology of Aquatic Vascular Plants. Edward Arnold Publishers, London.
Sebadduka, J., 2014. Mapping soil-landscape elements and the wetland in dambos and estimating CH4 and CO2 emissions fom dambo-terminated catena. Ph.D. thesis. Washington State University. UMI Number: 3640076.
Segers, R., 1998. Methane production and methane consumption: a review of processes underlying wetland methane fluxes. Biogeochemistry 41, 23–51. https://doi.org/10.1023/A:1005929032764.
Silva, T.S.F., Costa, M.P.F., Melack, J.M., 2010. Spatio-temporal variability of macrophyte cover and productivity in the eastern Amazon floodplain: a remote sensing approach. Remote Sens. Environ. 114, 1998–2010.
Silva, T.S.F., Melack, J.M., Novo, E.M.L., 2013. Responses of aquatic macrophyte cover and productivity to flooding variability on the Amazon floodplain. Glob. Change Biol. 19, 3379–3389.
Silva, T.S.F., Costa, M.P.F., Melack, J.M., Novo, E.M.L.M., 2008. Remote sensing of aquatic vegetation: theory and applications. Environ. Monit. Assess. 140, 131–145.
Silva, T.S.F., Melack, J., Streher, A.S., Ferreira-Ferreira, J., Furtado, L.F.A., 2015. Capturing the dynamics of Amazonian wetlands using synthetic aperture radar: Lessons learned and future directions. In: Tiner, R.W., Klemas, V., Lang, M.W. (Eds.), Advances in Wetland Classification and Mapping. Taylor and Francis Publ, pp. 455–472.
Simard, M., Pinto, N., Fisher, J.B., Baccini, A., 2011. Mapping forest canopy height globally with spaceborne lidar. J. Geophys. Res.: Biogeosci. 116, G04021. https://doi.org/10.1029/2011JG001708.
Sippel, S.J., Hamilton, S.K., Melack, J.M., Choudhury, B.J., 1994. Determination of inundation area in the Amazon River floodplain using the SMMR 37 GHz polarization difference. Remote Sens. Environ. 48, 70–76. https://doi.org/10.1016/0034-4257(94)90115-5.
Sjögersten, S., Black, C.R., Evers, S., Hoyos-Santillan, J., Wright, E.L., Turner, B.L., 2014. Tropical wetlands: a missing link in the global carbon cycle? Glob. Biogeochem. Cycles 28, 2014GB004844.
Sjögersten, S., Siegenthaler, A., Lopez, O.R., Aplin, P., Turner, B., Gauci, V., 2020. Methane emissions from tree stems in neotropical peatlands. N. Phytol. 225, 769–781.
Slagter, B., Tsendbazar, N.-E., Vollrath, A., Reiche, J., 2020. Mapping wetland characteristics using temporally dense Sentinel-1 and Sentinel-2 data: a case study in the St. Lucia wetlands, South Africa. Intern. J. Appl. Earth Obs. Geoinf. 86, 102009.
Somers, B., Asner, G.P., Tits, L., Coppin, P., 2011. Endmember variability in spectral mixture analysis: a review. Remote Sens. Environ. 115, 1603–1616.
Tanneberger, F., Tegetmeyer, C., Busse, S., Barthelmes, A., Shumka, S., Moles Mariné, A., Jenderedjian, K., Steiner, G.M., Essl, F., et al., 2017. The peatland map of Europe. Mires Peat 19, 1–17.
Terentieva, I., Glagolev, M., Lapshina, E., Sabrekov, A., Maksyutov, S., 2016. High resolution wetland mapping in West Siberian taiga zone for methane emission inventory. Biogeosciences 13, 4615–4626. https://doi.org/10.5194/bg-13-4615-2016.
Tiner, R.W., 2015. Classification of wetland types for mapping and large-scale inventories. In: Tiner, R.W., Lang, M.W., Klemas, V.V. (Eds.), Remote Sensing of Wetlands: Applications and Advances. CRC Press, Boca Raton, Florida, pp. 19–43.
Tiner, R.W., Lang, M.W., Klemas, V.V. (Eds.), 2015. Remote Sensing of Wetlands: Applications and Advances. CRC Press, Boca Raton, Florida.
Torbick, N., Chowdhury, D., Salas, W., Qi, J., 2017. Monitoring rice agriculture across Myanmar using time series Sentinel-1 assisted by Landsat-8 and PALSAR-2. Remote Sens 9, 119.
Tsendbazar, N., Herold, M., Li, L., Tarko, A., de Bruin, S., Masiliunas, D., Lesiv, M., Fritz, S., Buchhorn, M., Smets, B., 2021. Towards operational validation of annual global land cover maps. Remote Sens. Environ. 266, 112686.
Tulbure, M.G., Broich, M., Perin, V., Gaines, M., Ju, J., Stehman, S.V., Pavelsky, T., Masek, J.G., Yin, S., Mai, J., 2022. Can we detect more ephemeral floods with higher density harmonized Landsat Sentinel 2 data compared to Landsat 8 alone? ISPRS J. Photogramm. Remote Sens. 185, 232–246.
Umarhadi, D.A., Avtar, R., Widyatmanti, W., Johnson, B.A., Yunus, A.P., Khedher, K.M., Singh, G., 2021. Use of multifrequency (C-band and L-band) SAR data to monitor peat subsidence based on time-series SBAS InSAR technique. Land Degrad. Dev. 32, 4779–4794.
Ustin, S.L., Middleton, E.M., 2021. Current and near-term advances in Earth observation for ecological applications. Ecol. Process. 10, 1–57. https://doi.org/10.1186/s13717-020-00255-4.
Valley, R.D., Johnson, M.B., Dustin, D.L., Jones, K.D., Lauenstein, M.R., Nawrocki, J., 2015. Combining hydroacoustic and point-intercept survey methods to assess aquatic plant species abundance patterns and community dominance. J. Aquat. Plant Manag. 53, 121–129.
Venticinque, E., Forsberg, B., Barthem, R., Petry, P., Hess, L., Mercado, A., et al., 2016. An explicit GIS-based river basin framework for aquatic ecosystem conservation in the Amazon. Earth Syst. Sci. Data 8, 651–661.
Verhelst, K., Gou, Y., Herold, M., Reiche, J., 2021. Improving forest baseline maps in tropical wetlands using GEDI-based forest height information and Sentinel-1. Forests 12, 1374.
Villa, J.A., Ju, Y., Stephen, T., Rey-Sanchez, C., Wrighton, K.C., Bohrer, G., 2020. Plant-mediated methane transport in emergent and floating-leaved species of a temperate freshwater mineral-soil wetland. Limnol. Oceanogr. 65, 1635–1650.
Visser, F., Buis, K., Verschoren, V., Schoelynck, J., 2018. Mapping of submerged aquatic vegetation in rivers from very high-resolution image data, using object-based image analysis combined with expert knowledge. Hydrobiologia 812, 157–175. https://doi.org/10.1007/s10750-016-2928-y.
Wan, H., Qin, Z., Liu, Y., Xu, Y., 2010. Estimates of carbon fluxes from Poyang Lake wetlands vegetation in the growing season. In R.J. Frouin, H.R. Yoo, J.-S. Won and A. Feng (eds) Remote Sensing of the Coastal Ocean, Land, and Atmosphere Environment. Proc. SPIE 7858.
Wang, L., Dronova, I., Gong, P., Yang, W.B., Li, Y.R., Liu, Q., 2012. A new time series vegetation–water index of phenological–hydrological trait across species and functional types for Poyang Lake wetland ecosystem. Remote Sens. Environ. 125, 49–63. https://doi.org/10.1016/j.rse.2012.07.003.
Wang, Y., Filoso, S., Hess, L., Melack, J.M., 1995. Understanding the radar backscattering from flooded and nonflooded Amazonian forests: Results from canopy modeling. Remote Sens. Environ. 54, 324–332.
Wania, R., Ross, I., Prentice, I.C., 2010. Implementation and evaluation of a new methane model within a dynamic global vegetation model: LPJ-WHyMe v1. 3.1. Geosci. Model Dev. 3, 565–584.
Wania, R., Melton, J.R., Hodson, E.L., Poulter, B., Ringeval, B., Spahni, R., et al., 2013. Present state of global wetland extent and wetland methane modelling: methodology of a model inter-comparison project (WETCHIMP). Geosci. Model Dev. 6, 617–641.
Wassmann, R., Thein, U.G., Whiticar, M.J., Rennenberg, H., Seiler, W., Junk, W.J., 1992. Methane emissions from the Amazon floodplain: characterization of production and transport. Glob. Biogeochem. Cycles 6, 3–13.
Wdowinski, S., Hong, S.-H., 2015. Wetland InSAR: A review of the technique and applications, 2015. In: Tiner, R.W., Lang, M.W., Klemas, V.V. (Eds.), Remote Sensing of Wetlands: Applications and Advances. CRC Press, Boca Raton, Florida, pp. 137–154.
Wetzel, R.G., 2001. Limnology (chapter 18 – Land-water interfaces: Larger plants). Academic Press, New York.
Whitcomb, J., Moghaddam, M., McDonald, K., Kellndorfer, J., Podest, E., 2009. Mapping vegetated wetlands of Alaska using L-band radar satellite imagery. Can. J. Remote. Sens. 35, 54–72. doi: 10.5589/m08–080.
Whiting, G.J., Chanton, J.P., 1993. Primary production control of methane emissions from wetlands. Nature 364, 794–795.
Wohlfart, C., Winkler, K., Wendleder, A., Roth, A., 2018. TerraSAR-X and wetlands: a review. Remote Sens 10, 916.
Xavier, L., Becker, M., Cazenave, A., Longuevergne, L., Llovel, W., Rotunno Filho, O.C., 2010. Interannual variability in water storage over 2003-2008 in the Amazon Basin from GRACE space gravimetry, in situ river level and precipitation data. Remote Sens. Environ. 114, 1626–1637.
Xiao, D., Deng, L., Kim, D.-G., Huang, C., Tian, K., 2019. Carbon budgets of wetland ecosystems in China. Glob. Change Biol. 25, 2061–2076. https://doi.org/10.1111/gcb.14621.
Xu, P., Tsendbazar, N.E., Herold, M., Clevers, J.G.P.W., Li, L., 2022. Improving the characterization of global aquatic land cover types using multi-source Earth observation data. Remote Sens. Environ. 278, 113103.
Yamazaki, D., Ikeshima, D., Sosa, J., Bates, P.D., Allen, G.H., Pavelsky, T.M., 2019. MERIT Hydro: a high-resolution global hydrography map based on latest topography dataset. Water Resour. Res 55, 5053–5073. https://doi.org/10.1029/2019WR024873.
Yamazaki, D., Ikeshima, D., Tawatari, R., Yamaguchi, T., O'Loughlin, F., Neal, J.C., Sampson, C.C., Kanae, S., Bates, P.D., 2017. A high accuracy map of global terrain elevations. Geophys. Res. Lett. 44, 5844–5853. https://doi.org/10.1002/2017GL072874.
Zhang, B., Wdowinski, S., Gann, D., Hong, S.-H., Sah, J., 2022. Spatiotemporal variations of wetland backscatter: the role of water depth and vegetation characteristics in Sentinel-1 dual-polarization SAR observations. Remote Sens. Environ. 270, 112864.
Zhang, B., Tian, H., Lu, C., Chen, G., Pan, S., Anderson, C., et al., 2017. Methane emissions from global wetlands: an assessment of the uncertainty associated with various wetland extent data sets. Atmos. Environ. 165, 310–321 doi.org/10.1016/.
Zhang, B., Tian, H., Ren, W., Tao, B., Lu, C., Yang, J., Banger, K., Pan, S., 2016b. Methane emissions from global rice fields: Magnitude, spatiotemporal patterns, and environmental controls. Glob. Biogeochem. Cycles 30, 1246–1263. https://doi.org/10.1002/2016GB005381.
Zhang, Z., Zimmermann, N.E., Kaplan, J.O., Poulter, B., 2016a. Modeling spatiotemporal dynamics of global wetlands: comprehensive evaluation of a new sub-grid TOPMODEL parameterization and uncertainties. Biogeosciences 13, 1387–1408. https://doi.org/10.5194/bg-13-1387.
Zhang, Z., Poulter, B., Fluet-Chouinard, E., Jensen, K., McDonald, K., Hugelius, G., Gumbricht, T., Carroll, M., Prigent, C., Bartsch, A., 2021. Development and evaluation of the global wetland area and dynamics for methane modeling dataset (WAD2M). Earth Syst. Sci. Data 13, 2001–2023.